Structure of Fe(III) precipitates generated by the electrolytic dissolution of Fe(0) in the presence of groundwater ions

Case M. van Genuchten [a,*], Jasquelin Peña [b], Susan E. Amrose [a], Ashok J. Gadgil [a,c]

[a] *Department of Civil and Environmental Engineering, University of California, Berkeley, Berkeley, CA 94720, United States*
[b] *Institute of Earth Sciences, University of Lausanne, Lausanne, Switzerland*
[c] *Environmental Energy Technologies Division, Lawrence Berkeley National Laboratory, Berkeley, CA 94720, United States*

Abstract

We apply Fe K-edge extended X-ray absorption fine structure (EXAFS) spectroscopy and pair distribution function (PDF) analysis of high-energy X-ray scattering to investigate the effects of bivalent cation–oxyanion pairs on the structure of Fe(III) precipitates formed from the oxidation of Fe(II) generated by the electrolytic dissolution of Fe(0) electrodes. We found that Fe(II) oxidation in the presence of weakly adsorbing electrolytes (NaCl, $CaCl_2$, $MgCl_2$) leads to pseudo-lepidocrocite (Lp; γ-FeOOH), a poorly crystalline version of Lp with low sheet-stacking coherence. In the absence of bivalent cations, P and As(V) have similar uptake behavior, but different effects on the average Fe(III) precipitate structure: pseudo-Lp dominates in the presence of P, whereas a disordered ferrihydrite-like precipitate akin to hydrous ferric oxide (HFO) is the dominant phase that forms in the presence of As(V). Despite its lower affinity for Fe(III) precipitates, Si leads to Si-HFO in all conditions tested. The presence of 1 mM Ca^{2+} or Mg^{2+} enhances oxyanion uptake, destabilizes the colloidally stable oxyanion-bearing particle suspensions and, in some P and As(V) electrolytes, results in more crystalline precipitates. The trends in oxyanion uptake and Fe(III) precipitate structure in the presence of Ca^{2+}/Mg^{2+} suggest a systematic decrease in the strength of bivalent cation:oxyanion interaction in the order of $Ca^{2+} > Mg^{2+}$ and $P > As(V) \gg Si$. Using the PDF technique, we identify the polyhedral linkages that contribute to the intermediate structures (>6 Å) of disordered, nanoscale oxyanion-bearing Fe(III) precipitate samples. Our results suggest that oxyanions present during Fe(III) polymerization bind to corner-sharing Fe surface sites leading to a precipitate surface deficient in corner-sharing Fe, whereas the edge- and corner-sharing Fe sites in the precipitate core likely remain intact.

1. INTRODUCTION

Due to their large reactive surface area and high affinity for adsorbing contaminants and nutrients, Fe(III) (oxyhydr)oxides play an important role in controlling the fate and bioavailability of solutes in natural and engineered systems. For example, at natural Fe redox boundaries such as hyporheic zones and hydrothermal vents, Fe(III) (oxyhydr)oxides formed from Fe(II) oxidation efficiently immobilize contaminants and nutrients like P and Si (Kuhn and Sigg, 1993; Rancourt et al., 2001; Caetano and Vale, 2002). Electrocoagulation (EC) is an analogous engineered water treatment system that is based on the electrolytic dissolution of an Fe(0) anode, producing Fe(II), which is oxidized rapidly to insoluble Fe(III) by dissolved oxygen at

---

* Corresponding author. Address: 120 Blum Hall, University of California, Berkeley, Berkeley, CA 94720, United States. Tel.: +1 (510) 664 4343.

E-mail address: cmvangenuchten@berkeley.edu (C.M. van Genuchten).

near-neutral pH (Stumm and Lee, 1961; Lakshmanan et al., 2009). The Fe(III) ions polymerize in situ, creating Fe(III) precipitates with a high ion sorption affinity. The EC cell is akin to an engineered redox boundary where the rates of Fe(II) production and oxidation can be controlled, resulting in reactive Fe(III) precipitates (Li et al., 2012; van Genuchten et al., 2012). Electrocoagulation of Fe is also exploited for effective and low-cost water treatment of contaminants such as arsenic (Kumar et al., 2004; Lakshmanan et al., 2010; Amrose et al., 2013). Due to widespread arsenic contamination of groundwater, particularly in South Asia (Nordstrom, 2002), the uptake of arsenic during Fe(III) precipitation strongly motivates EC research.

By interfering with Fe(III) polymerization, ions common in natural waters (P, As(V), Si, Ca^{2+}, Mg^{2+}) can modify properties of the resulting precipitate such as the local bonding environment, mineral phase, crystallinity, and arsenic uptake mechanism (Waychunas et al., 1993; Rose et al., 1996; Doelsch et al., 2000; Pokrovski et al., 2003; Voegelin et al., 2010). Major dissolved species can also alter particle surface charge, which strongly influences particle aggregation and settling velocity (Sposito, 2008). These structural properties govern the macroscopic behavior and reactivity of Fe(III) (oxyhydr)oxides coprecipitated with arsenic and other ions. Therefore, knowledge of the structural effects and uptake behavior of major solutes is necessary to better understand contaminant and nutrient transport in natural systems. This information is also crucial to predict the performance of EC-based water treatment systems.

Bivalent cations (Ca^{2+}, Mg^{2+}) and oxyanions (P, As(V), Si) are ubiquitous in natural waters, yet their interdependent effects on the structure and reactivity of Fe(III) coprecipitates have only received attention recently. Voegelin et al. (2010) applied X-ray absorption spectroscopy (XAS) at the P, Ca, and Fe K-edges to investigate the formation of Fe(III) precipitates in the presence of Ca^{2+} and P at levels typical of South Asian groundwater. The authors showed that the tendency of P to form P–O–Ca linkages can reduce crystal growth poisoning normally caused by the formation of P–O–Fe bonds during P uptake. However, the interaction between Ca^{2+} and As(V) and its effect on Fe(III) polymerization in analogous Fe(III)–As(V)–Ca systems remain unclear. The observed increase in As(V) uptake by Fe(III) (oxyhydr)oxides in the presence Ca^{2+} has been attributed to several mechanisms ranging from the formation of direct Ca–O–As(V) linkages (Jia and Demopoulos, 2008; Guan et al., 2009; Kanematsu et al., 2013) to non-specific interactions such as Ca^{2+}-induced neutralization of particle surface charge (Wilkie and Hering, 1996; Stachowicz et al., 2008) or compression of the repulsive double layer (Masue et al., 2007). Some research has focused on the interaction of ion pairs involving Mg^{2+} or Si during adsorption to preformed Fe(III) minerals (Kanematsu et al., 2010, 2013; Stachowicz et al., 2008), but spectroscopic and X-ray scattering studies that probe systematically Fe(III) precipitate formation in binary electrolytes containing ion pairs involving either Mg^{2+} or Si (i.e. Mg–As(V), Mg–P, Si–Ca, Si–Mg) are largely absent from the literature.

In this research we begin by determining the macroscopic behavior and structure of EC precipitates generated in weakly-adsorbing background electrolytes. Next, we amend the electrolyte with a range of single oxyanion concentrations to compare the uptake and structural effects of P, As(V), and Si. Finally, we add either 1 mM Ca^{2+} or 1 mM Mg^{2+} to each of the single oxyanion electrolytes to investigate the bivalent cation–oxyanion interaction and its effect on the structure and reactivity of EC precipitates. By varying the composition of each electrolyte systematically, we can interpret the interaction of each ion pair (P–Ca, P–Mg, As(V)–Ca, As(V)–Mg, Si–Ca, Si–Mg) during Fe(II) oxidation and Fe(III) polymerization in model systems. Our study represents a significant contribution to understanding the formation of Fe(III) precipitates in more complex, but well defined binary electrolytes. These matrices may be more representative of natural systems than single solute electrolytes, but still permit the interpretation of the interdependent effects of each ion.

The structure and sorption reactivity of EC precipitates are investigated by integrating wet chemical measurements and complementary synchrotron-based X-ray techniques: Fe K-edge extended X-ray absorption fine structure (EXAFS) spectroscopy and pair distribution function (PDF) analysis of high-energy X-ray scattering data. EXAFS spectroscopy yields element-specific information that is limited to the short-ranged coordination about the absorbing atom (<6 Å). The PDF technique yields quantitative structural information from all atomic pairs within the coherently scattering structure and is thus sensitive to both short- and long-ranged order (Egami and Billinge, 2003; Proffen et al., 2003). Real-space resolution is also improved in the PDF due to the large scattering vector value accessible with high-energy X-rays (Petkov, 2005). However, the PDF technique is not element-specific and its fitting routine has been criticized as being poorly constrained, especially for nanocrystalline material (Manceau, 2009, 2011).

To more precisely guide the interpretation of EC precipitate characterization data, we report the EXAFS and PDF analyses of a suite of Fe(III) reference minerals. Pair distribution function refinements have been reported previously for 2-line ferrihydrite (Michel et al., 2007a, 2010), but not for goethite (α-FeOOH), lepidocrocite (γ-FeOOH), or scorodite ($FeAsO_4 \cdot 2H_2O$) to our knowledge. Our study is one of the few to date (Toner et al., 2012) to combine the EXAFS and PDF techniques to examine the local and intermediate-ranged structures of Fe(III) precipitate samples. Guided by the PDF refinements of reference minerals, we identify the Fe polyhedral connections (edge-/corner-sharing) that give rise to pair correlations beyond those reported previously for Fe(III) precipitates using EXAFS spectroscopy (>6 Å). Knowledge of the polyhedral linkages that contribute to the intermediate-ranged structure of our samples constrains and simplifies the interpretation of the EXAFS spectra, which is difficult to do for nanoparticles such as oxyanion-bearing HFO, where multiple overlapping scattering paths (e.g. edge-/corner-sharing Fe–Fe, Fe–P/As/Si) contribute to the broad second-shell peak in the Fourier transform.

2. MATERIALS AND METHODS

2.1. Preparation of electrolytes

Stock solutions of reagent grade $Na_2HAsO_4 \cdot 7H_2O$ (10 mM), $Na_2HPO_4 \cdot 7H_2O$ (10 mM), $Na_2SiO_3 \cdot 5H_2O$ (10 mM), $CaCl_2$ (100 mM), $MgCl_2 \cdot 6H_2O$ (100 mM), and NaCl (100 mM) were added to 18 MΩ Millipore water to generate all electrolytes. The concentrations of P, Si, Ca^{2+} and Mg^{2+} used in our study are chosen to represent typical values in South Asian groundwater (BGS, 2001). The As(V) concentrations reflect a range of values associated with arsenic-contamination from geogenic sources (e.g. South Asian groundwater, hydrothermal vents) (Rancourt et al., 2001; Rahman, 2002) and anthropogenic sources (e.g. metal refinement and mining activities) (Han et al., 2003). The sample naming convention followed in this work lists the initial amount of oxyanion (μM) in the electrolyte, along with the bivalent cation if present (i.e. sample As50+Ca represents the Fe(III) precipitates generated in an electrolyte containing initial concentrations of 50 μM As(V) and 1 mM Ca^{2+}). Samples generated in background electrolytes containing no oxyanions (NaCl, $CaCl_2$, $MgCl_2$) are herein designated as BgE samples. In experiments involving single oxyanions, 4 mM NaCl was added to facilitate charge transfer during electrolysis. The pH was adjusted to 7.5 ± 0.3 with 0.01 or 0.1 M NaOH or HCl prior to electrolysis under vigorous stirring, in part to prevent the formation of SiO_4 polymers in electrolytes containing Si (Roberts et al., 2004). According to speciation calculations preformed with Visual Minteq (Gustafsson, 2013) (see Section EA1 and Fig. EA1 of the Electronic Annex), the dominant forms of P, As(V), Si, and if present Ca^{2+} and Mg^{2+} are HPO_4^{2-} (~60–70%), $HAsO_4^{2-}$ (~85%), H_4SiO_4 (~100%), Ca^{2+} (~90–100%) and Mg^{2+} (85–100%), respectively.

2.2. Electrocoagulation experiments

The EC cell set-up is described in van Genuchten et al. (2012). Briefly, an acid-washed Fe(0) sheet anode (submerged surface area of 12 cm^2) and a Cu(0) mesh cathode spaced 1 cm apart were inserted into 500 mL of electrolyte. Precipitates were generated by applying a galvanostatic current under ambient atmospheric conditions. This cell configuration generates Fe(II) at the anode and $H_{2(g)}$ at the cathode (Lakshmanan et al., 2009; Li et al., 2012). The amount of Fe [mol] generated during EC is related to the current (i [C/s]) by Faraday's Law as follows: Fe $= (i \cdot t_e)/(n \cdot F)$, where t_e is the electrolysis time [s], n is the number of transferred electrons, and F is Faraday's constant (96485 C/mol) (Bard and Faulkner, 2001). For all experiments, a total iron concentration of 0.5 mM was generated at a current density (j, current per unit submerged area of electrode) of 2.5 mA/cm^2 and an iron dosage rate (D, amount of Fe added per time) of 0.83 μM/s.

After 10 min of electrolysis, the electrodes were removed and the suspension was allowed to react for 2 h under continuous stirring. Throughout the duration of the experiment, pH was measured and, if needed, adjusted to pH 7.5 ± 0.3. After the reaction stage, EC precipitates were separated from solution using 0.1 or 0.45 μm filters. The filtered solids of select samples were then prepared for characterization experiments. Concentrations of aqueous Fe, As, P, Si, Ca, and Mg in the initial electrolyte and clear filtrate were determined using a Perkin Elmer 5300 DV inductively coupled plasma optical emission spectrometer (ICP-OES). Solids ratios [mol:mol] were determined by taking the difference between measured values of the initial electrolyte and filtered solution normalized by the amount of added Fe. All experiments were replicated at least twice, with the chemical conditions used for most characterization experiments (Table 1) replicated at least three times. In separate experiments, after the 2 h reaction stage, the particle suspension was left to settle by gravity for 1 h (unstirred). An aliquot of sample was taken approximately 1–2 cm below the surface of the suspension using a wide-mouthed syringe before and after the 1 h settling time for turbidity measurements (Hach 2100 N Turbidimeter).

2.3. Synthesis of reference materials

Goethite (Goe; α-FeOOH), lepidocrocite (Lp; γ-FeOOH), and 2-line ferrihydrite (2LFh) were prepared following Schwertmann and Cornell (1991). Scorodite (Scor; $FeAsO_4 \cdot 2H_2O$) was synthesized following Paktunc et al. (2008). Details regarding the synthesis of these minerals appear in Section EA2.

2.4. Extended X-ray absorption fine structure spectroscopy

The mass of sample collected on filters as wet pastes was optimized for EXAFS measurements in transmission mode (Kelly et al., 2008). Spectra were collected at beam lines 4-1 and 4-3 of the Stanford Synchrotron Radiation Lightsource (SSRL, Menlo Park, CA) under typical ring conditions of 350 mA at 3.0 GeV. All samples were housed in a liquid nitrogen (77 K) cryostat during data collection. Fe K-edge spectra were simultaneously recorded in both transmission and fluorescence modes out to a reciprocal space value of 14–15 $Å^{-1}$. An Fe foil (7111.25 eV) was simultaneously measured during data collection to calibrate the X-ray energy. Second order harmonics were eliminated with harmonic rejection mirrors (4-3) or by detuning the Si(2 2 0) double crystal monochromator (phi 90) 20–40% (4-1).

Theoretical curve fitting was carried out from 1 to 4 Å in $R + \Delta R$-space using the SixPack software (Webb, 2005), which is based on IFEFFIT algorithms (Newville, 2001). Scattering paths used in the fits were derived from the first-shell Fe–O and second-shell edge- and corner-sharing Fe–Fe linkages of goethite (Gualtieri and Venturelli, 1999). An Fe–As scattering path corresponding to corner-sharing FeO_6 and AsO_4 polyhedra derived from the scorodite structure (Kitahama et al., 1975) was also used in the fits. In lieu of reporting the fit-derived coordination number (N), we opt to report the fit-derived amplitude (A), which is equivalent to the product of N and the passive electron reduction factor, S_0^2 (see Section EA3). Fitting variables typically included A, the change in threshold energy

Table 1
Names, initial compositions, and solids ratios for samples in EXAFS and PDF experiments.

Sample	Initial composition (μM)					Solids ratio (mol/mol)									
	As	P	Si	Ca	Mg	As	SD	P	SD	Si	SD	Ca	SD	Mg	SD
NaCl	–	–	–	–	–	–	–	–	–	–	–	–	–	–	–
CaCl$_2$	–	–	–	1000	–	–	–	–	–	–	–	0.10	0.06	–	–
MgCl$_2$	–	–	–	–	1000	–	–	–	–	–	–	–	–	0.26	0.04
As50	50	–	–	–	–	0.10	<0.01	–	–	–	–	–	–	–	–
As50+Ca	50	–	–	1000	–	0.10	<0.01	–	–	–	–	0.15	0.06	–	–
As50+Mg	50	–	–	–	1000	0.10	<0.01	–	–	–	–	–	–	0.18	*
As150	150	–	–	–	–	0.25	0.03	–	–	–	–	–	–	–	–
As150+Ca	150	–	–	1000	–	0.30	<0.01	–	–	–	–	0.21	0.08	–	–
As150+Mg	150	–	–	–	1000	0.29	<0.01	–	–	–	–	–	–	0.31	*
P50	–	50	–	–	–	–	–	0.09	<0.01	–	–	–	–	–	–
P50+Ca	–	50	–	1000	–	–	–	0.10	<0.01	–	–	0.12	*	–	–
P50+Mg	–	50	–	–	1000	–	–	0.10	<0.01	–	–	–	–	0.30	*
P150	–	150	–	–	–	–	–	0.23	0.03	–	–	–	–	–	–
P150+Ca	–	150	–	1000	–	–	–	0.29	<0.01	–	–	0.30	*	–	–
P150+Mg	–	150	–	–	1000	–	–	0.30	<0.01	–	–	–	–	0.35	*
Si250	–	–	250	–	–	–	–	–	–	0.21	0.02	–	–	–	–
Si250+Ca	–	–	250	1000	–	–	–	–	–	0.26	*	0.12	*	–	–
Si250+Mg	–	–	250	–	1000	–	–	–	–	0.25	*	–	–	0.21	*
Si7150	–	–	750	–	–	–	–	–	–	0.35	0.04	–	–	–	–
Si750+Ca	–	–	750	1000	–	–	–	–	–	0.46	0.06	0.20	0.07	–	–
Si750+Mg	–	–	750	–	1000	–	–	–	–	0.50	0.04	–	–	0.27	0.04

The "SD" column represents the standard deviation of the mean solids ratio of 3 or more replicates. Boxes with an (*) in the SD column highlight ions that were measured in duplicate.

(ΔE_0), interatomic distance (R), and the mean squared displacement parameter (σ^2). In addition to fitting reference minerals, we carried out shell-by-shell fits of the EXAFS spectra of representative samples (Section EA3 and Fig. EA2). The goodness-of-fit was evaluated using the R-factor or the reduced-chi-square (χ_v^2) value. A statistically significant change in the final χ_{vf}^2 value when compared with the initial final χ_{vi}^2 value is greater than two standard deviations (i.e. $(\chi_{vi}^2/\chi_{vf}^2) - 1 \geqslant 2(2/v)^{0.5}$, where v is the degrees of freedom) (Kelly et al., 2008). Additional details describing EXAFS sample preparation, data collection, reduction, and analysis are provided in Section EA3.

2.5. Pair distribution function analysis of high-energy X-ray scattering

High-energy X-ray scattering experiments were carried out on beam line 11 ID-B of the Advanced Photon Source at Argonne National Laboratory (ANL; Argonne, IL). Data were collected out to a Q value near 29 Å^{-1} at room temperature using 58.9 keV ($\lambda = 0.2128$ Å) X-rays. Measured scattering patterns corrected for sample-to-detector distance, tilt angle of the detector with respect to the direction of the incident beam, and X-ray polarization were integrated radially and converted to 1D plots of the scattering intensity versus scattering angle using the program Fit2D (Hammersley et al., 1996). The total structure function, $S(Q)$, and the PDF, $g(r)$, were obtained using the program PDFgetX2 (Farrow et al., 2007) using standard correction and normalization procedures, including those to correct for image-plate geometry (Chupas et al., 2003).

The starting structures used for the PDF refinements of reference materials were based on the crystal structure of goethite (Gualtieri and Venturelli, 1999), lepidocrocite (Wyckoff, 1963), 2-line ferrihydrite (Michel et al., 2007a) and scorodite (Kitahama et al., 1975). Structural variables refined over the R-range of 1–25 Å in the PDFs of crystalline reference minerals typically included the lattice constants (a, b, c), isotropic displacement parameters (U), and scale factor. For the refinement of 2LFh, the lattice constants, atomic positions and site occupancies, U values, and correlated atomic motion (δ) value were taken from a previous 2LFh refinement (Michel et al., 2007a) and were held constant while the scale factor, and peak broadening (Q_{broad}) were refined over the R-range of 1–20 Å. The goodness-of-fit for all refinements was evaluated using the weighted agreement factor, R_w (Egami and Billinge, 2003). Additional information regarding data collection and our analysis routine appear in Section EA4 of the Electronic Annex.

3. RESULTS

3.1. Macroscopic properties of EC precipitate suspensions

3.1.1. Turbidity

The initial and final turbidity of a subset of EC precipitate samples, together with the corresponding oxyanion percent removal from the supernatant solution, appear in Fig. 1. The suspension of precipitates generated in the weakly-adsorbing background electrolytes (BgE; NaCl, CaCl$_2$, MgCl$_2$) is dark orange with high initial turbidity

after the reaction. The large aggregated flocs settle quickly leading to <1 NTU final turbidity after 1 h of settling (Fig. 1). When filtered and dried, the BgE samples form densely-aggregated, dark red spherical particles. Variations in the initial turbidity of EC precipitate samples with similar mass but different chemical composition may be explained by floc density, a property to which turbidity measurements are insensitive. In contrast to the BgE samples, the presence of oxyanions leads to translucent light yellow suspensions with no visible flocs and lower initial turbidity. The colloidally stable suspensions generated in electrolytes containing initial concentrations of 150 µM P, 150 µM As(V), or 750 µM Si (i.e. samples P150, As150, Si750) showed little change in turbidity after the 1 h settling time. The presence of 1 mM Ca^{2+} or Mg^{2+} in the oxyanion electrolyte samples leads to cloudy suspensions with a greater initial turbidity than the individual oxyanion samples, but smaller visible flocs than the BgE suspensions. The low turbidity in these samples after 1 h of settling indicates that bivalent cations promote the aggregation of crystallites into visible flocs that settle quickly, even in the presence of high levels of oxyanions. When filtered and dried, the high oxyanion-bearing samples form thin, beige flakes that were visually observed to be loosely aggregated.

3.1.2. Ion uptake and molar composition of EC precipitates

Fig. 2 presents ion removal as a function of initial oxyanion concentration in the presence or absence of 1 mM Ca^{2+} or Mg^{2+}. In the absence of Ca^{2+} or Mg^{2+}, P and As(V) exhibit similar removal behavior. Around 90% removal of both P and As(V) is obtained for initial P or As(V) $\leqslant 100$ µM (P50, P100, As50, As100 samples), whereas a significant fraction of P or As(V) remains in solution as the initial concentration increases. Normalizing P or

As(V) removal by the 0.5 mM Fe dosed leads to solid ratios ranging from 0.09 to 0.4 mol:mol for initial P or As(V) values of 50–500 µM. In contrast, a significant fraction of Si remains in solution after the reaction in all conditions with and without Ca^{2+} or Mg^{2+}. Lower solids ratios for Si (0.06–0.35 mol:mol for initial concentrations of 50–750 µM) are observed than for the same initial P or As(V) concentrations, confirming the weaker affinity of Si for Fe(III) mineral surfaces (Roberts et al., 2004).

The presence of Ca^{2+} or Mg^{2+} enhances both P and As(V) removal, but this effect is larger for P than As(V), especially at higher initial oxyanion concentrations. The addition of 1 mM Ca^{2+} leads to >90% P removal for all conditions tested. The corresponding uptake of Ca^{2+} also increases with initial P, approaching 1:1 stoichiometric removal of Ca^{2+} and P at the highest initial P values. Although Mg^{2+} also enhances P removal, the effect is less pronounced. Only 70% removal of the highest initial P value is observed in the presence of Mg^{2+}, and the corresponding removal of Mg^{2+} is not stoichiometric.

The As(V):Fe solids ratio at the highest initial As(V) concentration increases by approximately 66% in the presence of Ca^{2+}, but over 30% of the initial 500 µM As(V) concentration remains in solution after the reaction. The corresponding uptake of Ca^{2+} increases with initial As(V), reaching 1.4 and 1.5 As(V):Ca^{2+} for the highest As(V) samples. The presence of Mg^{2+} enhances As(V) removal, and the corresponding removal of Mg^{2+} increases with initial As(V), but both to a lesser extent than Ca^{2+}.

The presence of Ca^{2+} or Mg^{2+} enhances Si removal by only a small percentage and there is no significant difference between the effects of Ca^{2+} versus Mg^{2+}. In line with this result, the uptake of both Ca^{2+} and Mg^{2+} does not vary significantly over the large range of initial Si concentrations
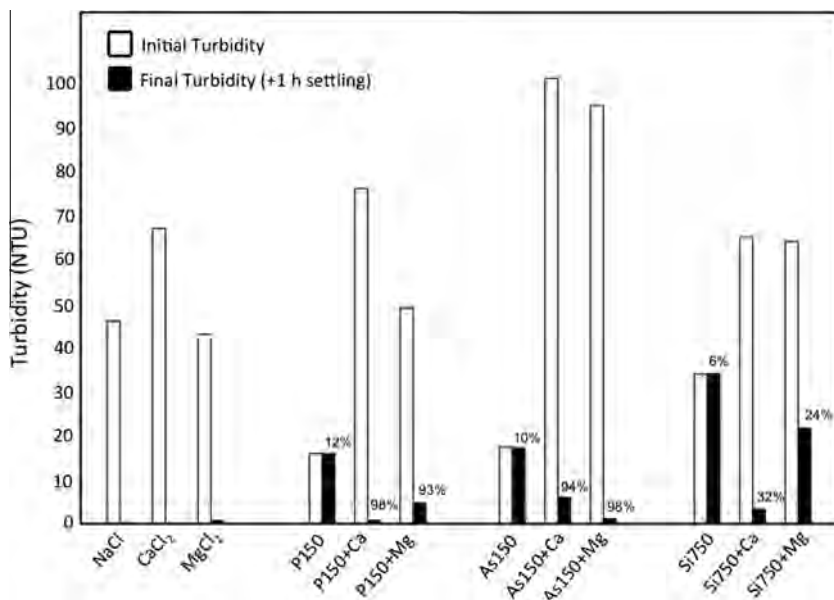

Fig. 1. Turbidity measurements as a function of the electrolyte chemistry. Initial turbidity measurements (open bars) were taken immediately after 2 h reaction stage. Final turbidity measurements (solids bars) were taken after 1 h of settling (the x-axis thickness obscures the final turbidity in the NaCl and $CaCl_2$ samples). Percentages above final turbidity indicate oxyanion removal in the supernatant solution.

(50–750 μM). The insignificant roles of Ca^{2+} and Mg^{2+} on Si removal, and vice versa, suggest there is not a strong direct interaction between Si and Ca^{2+}/Mg^{2+}.

3.2. Structural characterization of reference materials

In this section, we relate the crystal structure of each reference mineral to characteristic features in the characterization data. Images of the polyhedral structures of each investigated reference mineral along with a brief description of important structural features are given in Fig. 3. Fig. 4a and b overlay the EXAFS spectra and their Fourier-transforms, respectively, on top of the shell-by-shell fits. The PDFs of reference material are overlain to the refinements and are also separated into their partial component PDFs in Fig. 4c. A summary of the EXAFS and PDF fitting parameters is given in the EA.

3.2.1. Goethite

Goethite (Goe) consists of bands of edge-sharing FeO_6 octahedra, with each band oriented to share corners, forming tunnels that are bridged by H atoms (Fig. 3) (Schwertmann and Cornell, 1991). Each FeO_6 octahedron in the Goe crystal consists of different Fe–O distances ranging from 1.93 to 2.14 Å. The FeO_6 octahedra of Goe are connected by three distinct linkages, giving rise to three next nearest-neighbor Fe–Fe distances: $R_{Fe–Fe1} = 3.02$ Å for single edge-sharing, $R_{Fe–Fe2} = 3.29$ Å for double-edge sharing, and $R_{Fe–Fe3} = 3.43$ Å for corner-sharing FeO_6 octahedra.

The partial PDFs (Fig. 3c) verify the Fe–O, edge-sharing Fe–Fe and corner-sharing Fe–Fe peaks near 2.0, 3.0 Å and 3.4 Å, respectively. The subtle asymmetry at lower R in the corner-sharing Fe–Fe peak at 3.4 Å is consistent with the overlapping edge-sharing Fe–Fe pair at ~3.3 Å identified from the shell-by-shell EXAFS fits (Table EA1). The most intense peak in the PDF at approximately 5.4 Å is primarily due to Fe–Fe correlations. The crystal structure of Goe contains 14 different Fe–Fe atomic pairs in the range of 5.3–5.5 Å. Two of these 14 Fe–Fe pairs exist exclusively within the band of single and double edge-sharing FeO_6 octahedra, whereas the remaining 12 pairs (85% of the Fe–Fe pairs at this distance) contain a contribution from corner-sharing FeO_6 octahedra. Thus, in addition to the direct corner-sharing peak near 3.4 Å, we consider the peak near 5.4 Å diagnostic of corner-sharing FeO_6 octahedra.

3.2.2. Lepidocrocite

The basic building block of lepidocrocite (Lp) is a band of edge-sharing FeO_6 octahedra similar to Goe, but in Lp, individual bands are linked together through additional edge-sharing connections to produce zig-zagging sheets (Fig. 3) (Wyckoff, 1963). The two types of edge-sharing linkages in Lp result in edge-sharing Fe–Fe distances at 3.05 and 3.06 Å. The corrugated edge-sharing FeO_6 octahedral sheets in Lp are offset from one another by approximately 6.4 Å in the (0 0 1) direction and are held together by H-bonds, resulting in sheet stacking along the c-axis direction (Wyckoff, 1963).

Consistent with the Fourier-transformed EXAFS spectrum, the dominant features of the Lp PDF at low R
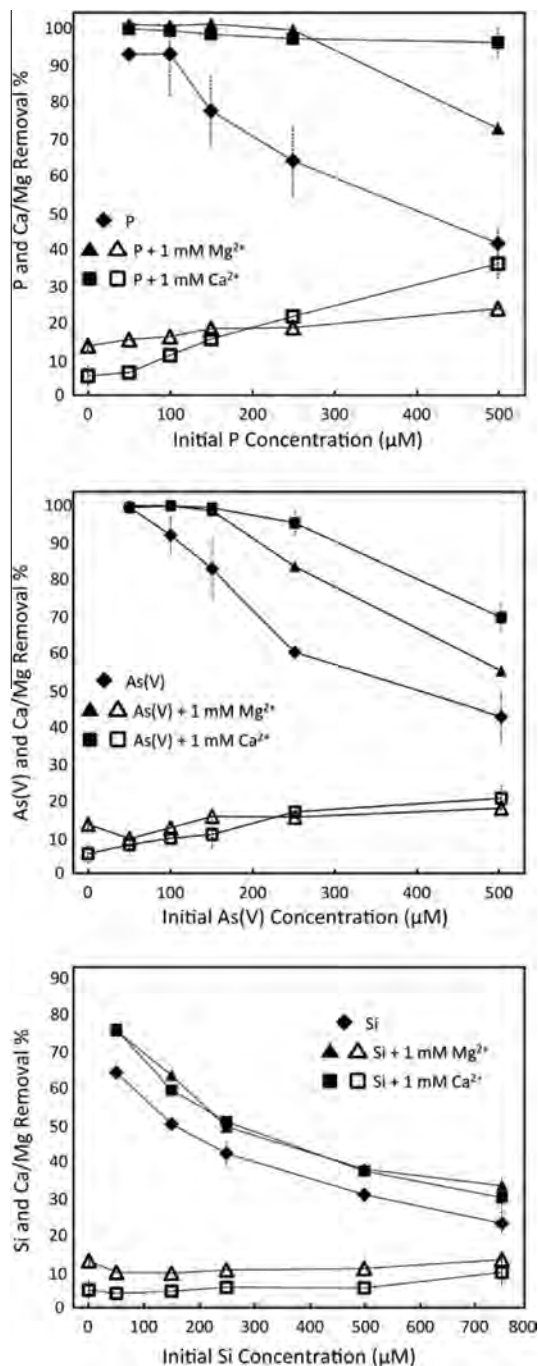

Fig. 2. Removal percentages of oxyanions and bivalent cations as a function of initial oxyanion concentration. Solid symbols represent oxyanion removal percentage, while open symbols represent bivalent cation removal percentage. Error bars represent the standard deviation of the mean of replicate experiments.

include two peaks near 2.0 and 3.0 Å, which are assigned to Fe–O and Fe–Fe atomic pairs of edge-sharing FeO_6 octahedra. Based on the partial PDFs, the Fe–O peak at 4.2 Å and Fe–Fe peak at 5.2 Å can be assigned to atomic pairs within an octahedral sheet (i.e. intra-sheet atomic pairs). The differences in the shape of the Lp PDF in the region from 6.4 to 9.2 Å compared to the other Fe reference

materials identify this region of the PDF as a fingerprint for Lp. The Fe–Fe contribution to the peak near 8.6 Å arises exclusively from inter-sheet Fe–Fe atomic pairs. Accordingly, the amplitude of this peak can be used to approximate the extent of coherent sheet-stacking in Lp.

3.1.3. 2-Line ferrihydrite

Currently, two structural models are cited for 2-line ferrihydrite (2LFh). The two models differ primarily in that the model of Michel et al. (2007a) describes 2LFh as a single phase consisting of approximately 20% tetrahedral Fe (^{IV}Fe), whereas the model of Drits et al. (1993) consists of entirely octahedral Fe (^{VI}Fe) in the form of three different phases. The confirmation of ^{IV}Fe in 2LFh has been reported by independent research groups using Fe K-edge XAS, Fe L-edge XAS, neutron scattering, and X-ray magnetic circular dichromatism (Harrington et al., 2011; Maillot et al., 2011; Guyodo et al., 2012; Peak and Regier, 2012), although these studies have been disputed in recent work (Manceau, 2011, 2012; Manceau and Gates, 2013; Paktunc et al., 2013). However, there seems to be a growing consensus of the use of the Michel model for 2LFh (Cismasu et al., 2011, 2012; Dyer et al., 2012; Toner et al., 2012). In this work, we use the Michel model as a starting point to identify characteristic features present in the PDFs of the samples.

The Michel model of 2LFh consists of Fe atoms in different coordination environments occupying multiple sites. Edge-sharing FeO_6 octahedra ($^{VI}Fe_E$, site Fe1: $R_{Fe-Fe} = 2.94$–3.02 Å) form an octahedral sheet similar to Lp, but in 2LFh, each edge-sharing sheet contains a six-membered ring vacancy (Fig. 3). Either a second FeO_6 octahedron ($^{VI}Fe_C$, site Fe2: $R_{Fe-Fe} = 3.50$ Å) or an FeO_4 tetrahedron ($^{IV}Fe_C$, site Fe3: $R_{Fe-Fe} = 3.39$ Å) sits atop the vacancy and shares corners with multiple $^{VI}Fe_E$ octahedra of the six-membered ring vacancy site. The Fe polyhedra that occupy the vacancy sites link together octahedral sheets by sharing either edges ($R_{Fe-Fe} = 3.13$ Å) or corners ($R_{Fe-Fe} = 3.31$ Å) with $^{VI}Fe_E$ octahedra of a different sheet.

The peaks in the 2LFh PDF are broader than for the other reference materials, pointing to the disordered nature of 2LFh. In contrast to the PDFs of Lp and Goe, the oscillations in 2LFh disappear near 2.0 nm. This peak decay is within the instrumental resolution (see Section EA4), indicating that the range of structural coherence in 2LFh is near 2.0 nm, consistent with previous studies (Michel et al., 2007b; Toner et al., 2012). To most accurately assign peaks in the complete PDF, the partial Fe–O and Fe–Fe PDFs were subdivided (Fig. 5) into the three Fe sites described above: octahedral edge-sharing $^{VI}Fe_E$, octahedral corner-sharing $^{VI}Fe_C$, and tetrahedral corner-sharing $^{IV}Fe_C$. Consistent with our shell-by-shell EXAFS fits (Table EA3), the first Fe–O and Fe–Fe peaks in the PDF (<4 Å) are due to the first and second shell of Fe polyhedra sharing edges and corners. An intermediate-ranged fingerprint of 2LFh appears in the region from 4.0 to 7.0 Å and includes three characteristic peaks near 4.7, 5.3, 6.2 Å, with a smaller peak around 6.8 Å (herein denoted as Fh1, Fh2, Fh3, and Fh4; see Table 2 and Fig. 5). Peaks Fh1 and Fh3 are due primarily to Fe–O pairs exclusive to the edge-sharing octahedral sheet (i.e. $^{VI}Fe_E$), whereas peaks Fh2 and Fh4 arise primarily due to corner-sharing Fe polyhedra (i.e. $^{VI}Fe_C$ and $^{VI}Fe_E$). Based on the 2LFh model refinement, Fe atoms contained exclusively in the octahedral sheet of 2LFh cannot produce the four peaks in the 2LFh fingerprint without some corner-sharing Fe polyhedra.
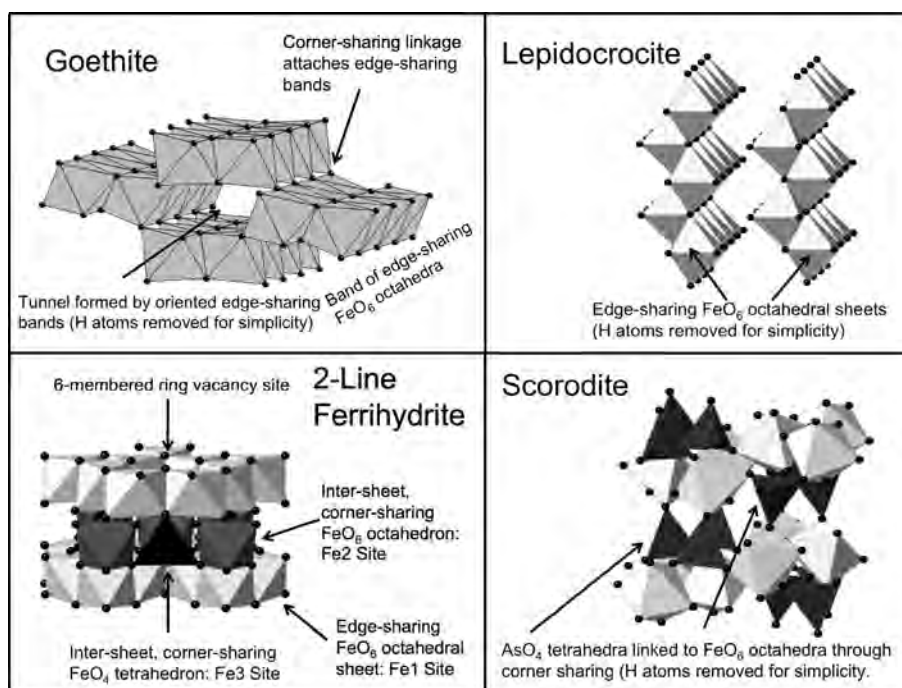

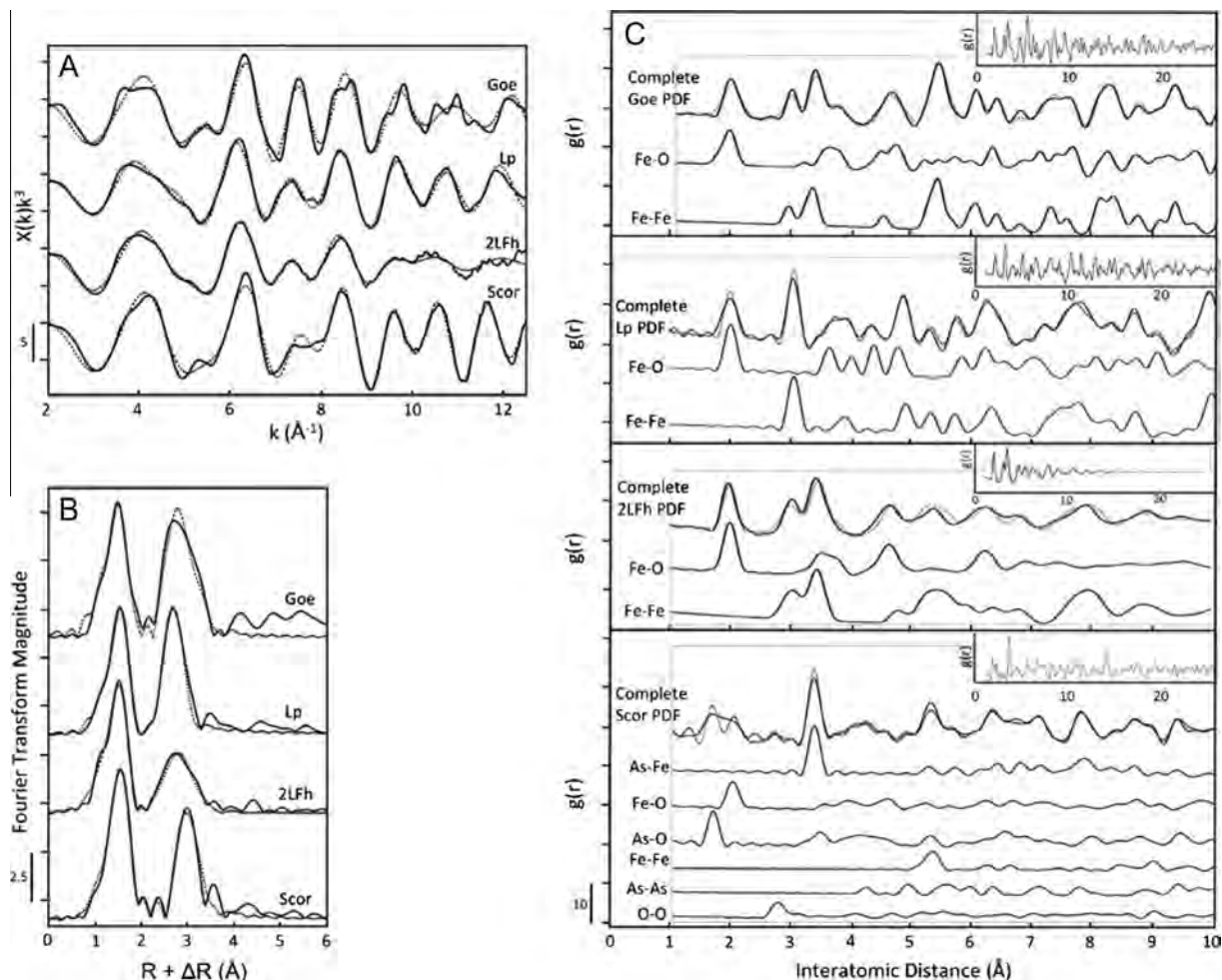Fig. 3. Polyhedral representations of reference materials.

Fig. 4. (A) Fe K-edge EXAFS spectra, (B) Fourier-transformed Fe K-edge EXAFS spectra, and (C) complete and partial pair distribution functions (PDF) of reference Fe minerals. The output from PDF refinements and shell-by-shell EXAFS fits appear as dotted lines while all experimental data appear as solid black lines. The inset in (C) shows the PDFs extended out to approximately 2.5 nm.

3.2.4. Scorodite

In the mineral scorodite (Scor), each corner of an AsO_4 tetrahedron ($R_{As-O} = 1.68$–1.69 Å) is linked to the corner of an FeO_6 octahedron ($R_{Fe-O} = 1.68$–1.69 Å). The two remaining uncoordinated vertices of the FeO_6 octahedron are bound to two hydrogen atoms (Kitahama et al., 1975). No direct edge- or corner-sharing Fe–Fe (or As–As) linkages exist in the mineral. Thus, the major polyhedral linkage consists of corner-sharing AsO_4 and FeO_6 polyhedra ($R_{Fe-As} = 3.34$–3.39 Å). Although Scor contains direct bonding between AsO_4 and FeO_6 polyhedra, the dominant coordination environments of Fe and As(V) are different than observed for As(V) adsorbed to Fe(III) (oxy-hydr)oxides in the ^2C geometry, where R_{As-Fe} is 3.25 Å instead of approximately 3.36 Å as found in Scor (Sherman and Randall, 2003).

The PDF of Scor shows scattering from atomic pairs involving both As and Fe atoms. The peak near 1.7 Å in the PDF is due to As–O pairs of the AsO_4 tetrahedron. The next two peaks at approximately 2.0 and 3.4 Å in the Scor PDF are consistent with the Fe–O and Fe–As pairs

identified in the Fourier-transformed EXAFS spectrum (Table EA1). The intense peak near 5.5 Å is mainly due to Fe–Fe pairs; no peak is due to As–As pairs only. Most intermediate-ranged peaks are mixtures of the atomic pairs present in Scor.

3.3. Background electrolytes

The Fe K-edge EXAFS spectra, Fourier transforms and PDFs of the BgE samples (NaCl, $CaCl_2$ and $MgCl_2$) as well as Lp and 2LFh appear in Fig. 6.

3.3.1. EXAFS spectroscopy

The EXAFS spectra of the BgE samples display features similar to that of Lp, such as the broadened asymmetric first oscillation between 3 and 5.5 Å^{-1}. The few differences between the EXAFS spectra of BgE samples relative to that of Lp include the slightly reduced oscillation near 6.1 Å^{-1}, the absence of the subtle shoulder in the oscillation at 7.5 Å^{-1}, and the reduced amplitude of the two oscillations between 9 and 11 Å^{-1}. As shown in the Fourier-transformed
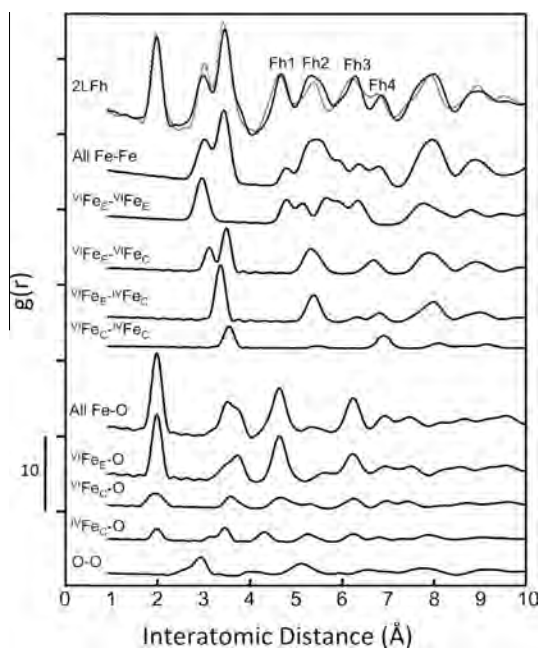
Fig. 5. Partial component pair distribution functions of 2LFh. In the Michel model of 2LFh, site Fe1 is $^{VI}Fe_E$, site Fe2 is $^{VI}Fe_C$, and site Fe3 is $^{IV}Fe_C$. Fh1, Fh2, Fh3 and Fh4 indicate peaks in the 2LFh fingerprint. The PDF refinement appears as a solid black line and the experimental PDF appears as a dotted black line.

EXAFS spectra, the short-ranged structures of Lp and the BgE samples are generally similar and consist of comparable contributions of Lp-like Fe–O and edge-sharing Fe–Fe scattering.

3.3.2. Pair distribution function

Consistent with Lp, two peaks attributed to Fe–O and edge-sharing Fe–Fe atomic pairs dominate the BgE sample PDFs at $R < 4$ Å. Beyond 4 Å, the BgE sample PDFs begin to show differences in relative peak amplitude and breadth compared to the Lp PDF. Fig. 6 shows the calculated PDFs derived from a supercell (see Section EA4) of model Lp nanoparticles with one, two, and three coherently stacked edge-sharing FeO_6 sheets along with the calculated PDF of an "ideal" periodic Lp crystal extending out to infinity in all directions.

The calculated double-sheet PDF reproduces almost all intermediate-ranged peaks of the BgE sample PDFs better

than the single-sheet, triple-sheet, or periodic models. Comparison between the single-sheet model PDF and the periodic Lp model PDF suggests that peak Lp1 near 5.8 Å and peak Lp3 near 7.2 Å correspond to scattering within a single sheet, whereas peak Lp2 near 6.2 Å and peak Lp4 near 8.6 Å correspond to scattering between individual sheets. Beyond 10 Å, the double-sheet calculation also most accurately reproduces the sample PDFs (see inset of Fig. 6).

Although all of the PDFs for the BgE samples are similar, some differences exist. The first and second nearest-neighbor atomic correlations in the $MgCl_2$ sample PDF are similar to the other samples in relative height, but the absolute magnitude of these peaks in the $MgCl_2$ sample PDF is reduced. The majority of the peaks beyond 4 Å in the $MgCl_2$ sample PDF are broader and less intense than the PDFs of NaCl and $CaCl_2$ samples, suggesting reduced intermediate ordering. Additionally, the amplitudes of the peaks in the $MgCl_2$ sample (Fig. 6 inset) decay at lower R than the NaCl and $CaCl_2$ samples, pointing to a smaller coherent scattering domain (CSD) in the $MgCl_2$ sample. The apparent reduction in crystallinity in the $MgCl_2$ sample can be rationalized by the higher uptake of Mg^{2+} relative to Ca^{2+} and the consequent disruption of Fe bonding in these samples, which is consistent with the adsorption behavior of Mg^{2+} and Ca^{2+} to Fe(III) minerals at circumneutral pH (Sverjensky, 2006; Kanematsu et al., 2013).

3.4. Phosphate concentration series

3.4.1. EXAFS spectroscopy

Fig. 7 displays the Fe K-edge EXAFS spectra of the P concentration series (P50, P50+Ca, P50+Mg, P150, P150+Ca, and P150+Mg) alongside the Lp and 2LFh references. The EXAFS spectra for the P50, P50+Ca and P50+Mg samples share similar features to the EXAFS spectra of the BgE samples including the broadened first oscillation between 3 and 5.5 Å^{-1}. Among these three low P samples, Ca^{2+} or Mg^{2+} does not significantly alter the line shape or phase of any of the oscillations. Two peaks of similar amplitude due to Fe–O and edge-sharing Fe–Fe scattering dominate the Fourier-transformed EXAFS spectra of the low P samples, consistent with Lp and the BgE samples.

Small differences exist between the EXAFS spectra of the high initial P samples (P150, P150+Ca and P150+Mg) and the BgE samples. The first oscillation in the EXAFS spectra of the P150 and P150+Mg samples lack the broad shoulder characteristic of Lp. Additionally, the

Table 2
Identification of peak fingerprints in 2LFh and Lp PDFs.

2LFh peak ID	R (Å)	Atomic pair(s)	Primary contributions	Lp peak ID	R (Å)	Atomic pair(s)	Primary contributions
Fh1	4.7	Fe–O	$^{VI}Fe_E$–O	Lp1	5.8	Fe–O and Fe–Fe	Inter-sheet
Fh2	5.3	Fe–Fe	$^{VI}Fe_E$–$^{VI}Fe_C$ and $^{VI}Fe_E$–$^{IV}Fe_C$	Lp2	6.2	Fe–O and Fe–Fe	Intra-sheet
Fh3	6.2	Fe–O	$^{VI}Fe_E$–O	Lp3	7.2	Fe–O and Fe–Fe	Intra-sheet
Fh4	6.8	Fe–Fe	$^{VI}Fe_E$–$^{VI}Fe_C$	Lp4	8.6	Fe–Fe	Inter-sheet

Peak identification is based on PDF refinements of reference 2LFh (Michel et al., 2007a) and Lp (Wyckoff, 1963).
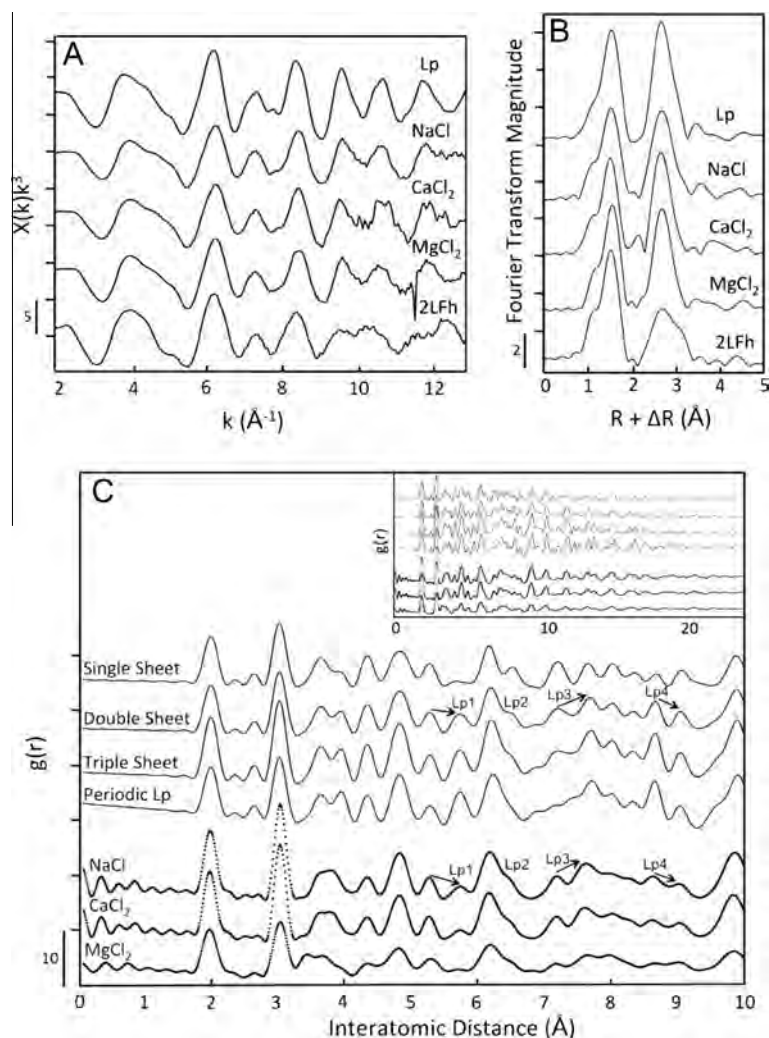
Fig. 6. (A) Fe K-edge EXAFS spectra, (B) Fourier-transformed EXAFS spectra, and (C) PDFs of precipitates generated in background electrolytes (NaCl, CaCl$_2$, and MgCl$_2$;BgE samples). The top four PDFs in (C) are calculated based on the crystal structure of Lp using models clusters containing one, two, three and an infinite number of coherently stacked sheets. The bottom three PDFs in (C) are experimental data. Lp1, Lp2, Lp3, and Lp4 highlight characteristic peaks in both the experimental and calculated PDFs that differ from peaks in an "ideal" lepidocrocite crystal (Periodic Lp). Arrows in (C) denote changes in relative peak intensities that are indicative of changes in sheet stacking order. The inset in (C) shows the PDF extended out to 2.5 nm.

broadened oscillations beyond approximately 8.5 Å^{-1} in these two samples begin to resemble the 2LFh EXAFS spectrum. In contrast, the P150+Ca sample resembles the EXAFS spectra of the low P and BgE samples, suggesting the presence of Ca^{2+} leads to a more Lp-like average local structure. Consistent with higher Fe–Fe ordering in the P150+Ca sample, the second-shell peak amplitude of the Fourier transform is increased relative to those of the P150 and P150+Mg samples.

3.4.2. Pair distribution function

All PDFs in the P series (Figs. 8 and 9) contain Lp-like signatures to varying extents. Fe–O and edge-sharing Fe–Fe peaks dominate the short-ranged region (<4 Å) of the P50, P50+Ca and P50+Mg PDFs. The reduced intensity of sheet-stacking peaks Lp1 and Lp4 in the low P PDFs

suggests that these samples contain less sheet-stacking order than Lp, and in some cases, less than the BgE samples. Although it is not possible to quantify the average number of coherently-stacked sheets in the low P samples, the trends suggest single- and double-stacked sheets.

The PDFs of the high P samples (150P, 150P+Ca and 150P+Mg) contain a peak near 1.5–1.6 Å consistent with P–O scattering from PO$_4$ tetrahedra. These samples also contain amplitude from 3.2 to 3.6 Å that is absent from the Lp PDF, which may be due to a minor fraction of corner-sharing Fe or Fe–P pairs of sorbed PO$_4$, ($R_{\text{Fe–P}}$ of 3.2–3.3 Å for sorbed PO$_4$ or amorphous Fe(III)-phosphate (Rose et al., 1996, 1997) (Voegelin et al., 2010)). The three peaks from 4.0 to 5.5 Å in the high P samples are broadened and the Lp1 and Lp4 sheet-stacking peaks are reduced compared to the low P samples. The peak amplitudes of the
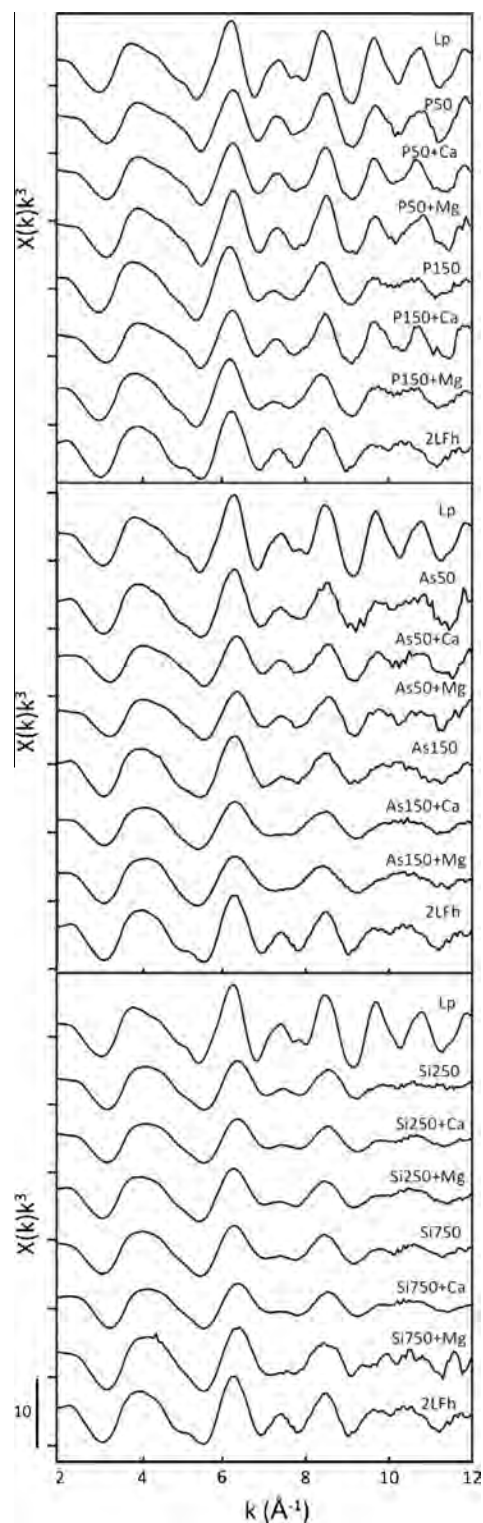
Fig. 7. (A) Fe K-edge EXAFS spectra of precipitate samples generated in electrolytes containing P, As(V), or Si in the presence or absence of 1 mM CaCl$_2$ or 1 mM MgCl$_2$. Spectra for Lp and 2LFh accompany each concentration series to aid fingerprinting of characteristic line shapes.

P150+Mg PDF appear to decay at lower R than both the high P samples and 2LFh, suggesting that the CSD of the
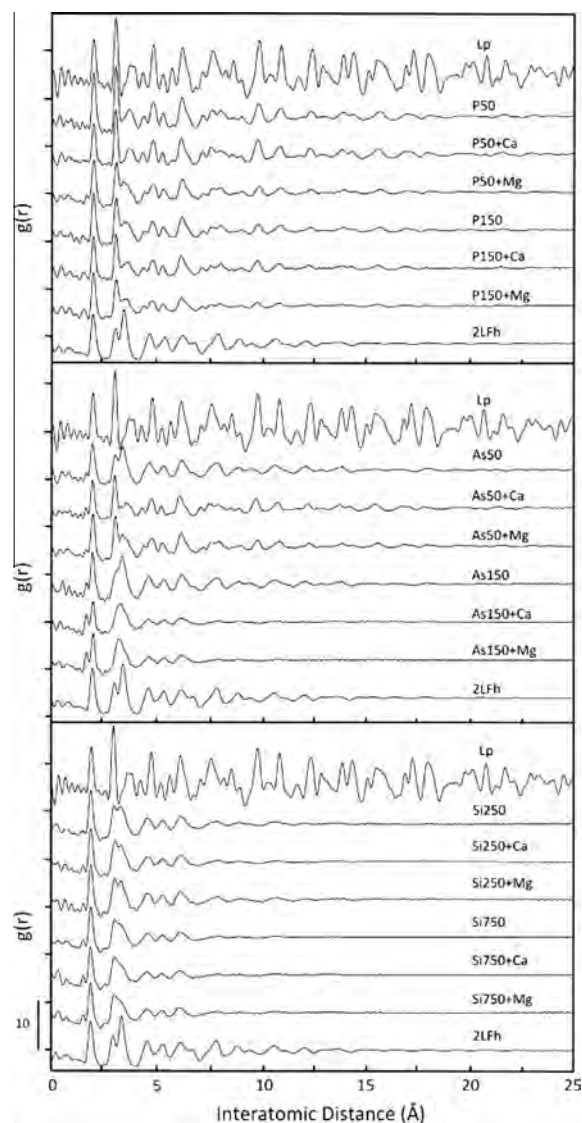

Fig. 8. Pair distribution functions (PDFs) of precipitate samples generated in electrolytes containing P, As(V), or Si in the presence or absence of 1 mM CaCl$_2$ or 1 mM MgCl$_2$. The PDFs for Lp and 2LFh accompany each concentration series to aid fingerprinting of characteristic peak positions and magnitudes.

P150+Mg sample is less than the 2.0 nm CSD typically reported for of 2LFh (Michel et al., 2007b).

3.5. Arsenate concentration series

3.5.1. EXAFS spectroscopy

Fig. 7 presents the Fe K-edge EXAFS spectra of the As(V) concentration series. The line shape and phase of the As50 EXAFS spectrum, including the symmetric first-oscillation between 3 and 5.5 Å^{-1} and small hump near 5.3 Å^{-1}, resemble that of 2LFh, whereas the asymmetric first oscillation in the EXAFS spectra of the As50+Ca and As50+Mg samples resembles that of Lp. The 2nd:1st shell peak amplitude ratio is larger in the As50+Ca and As50+Mg samples relative to the As50 sample, suggesting
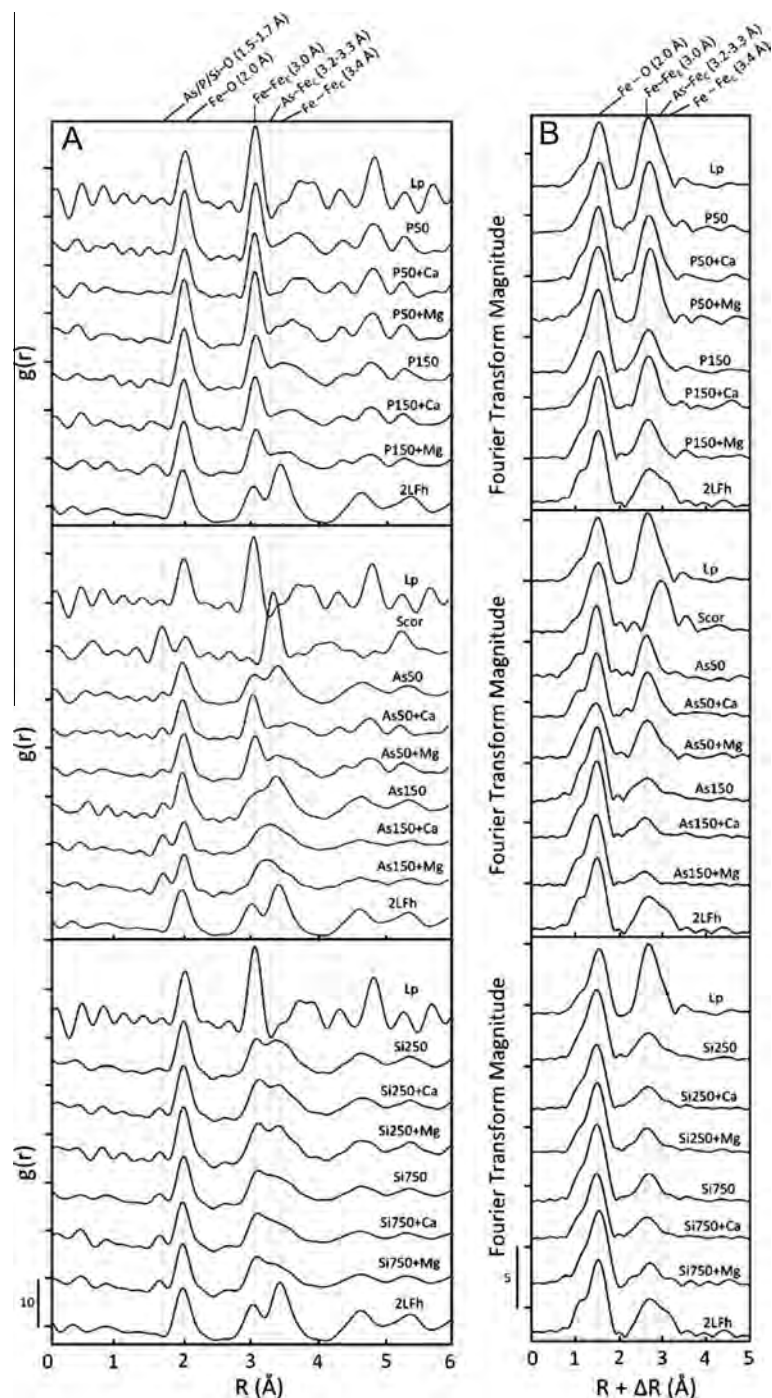
Fig. 9. Comparison of the local structures (first few coordination spheres) of identical samples using (A) the PDF and (B) EXAFS techniques. The vertical lines highlight peaks due to atomic pairs from P/As(V)/Si–O, Fe–O, Fe–Fe$_E$ (edge-sharing Fe octahedra), Fe–As$_C$ (corner-sharing AsO$_4$ and FeO$_6$ polyhedra), and Fe–Fe$_C$ (corner-sharing Fe polyhedra).

an increase in local Fe–Fe coordination in these two samples.

The EXAFS spectra of the high As(V) samples all exhibit features observed in the EXAFS spectrum of 2LFh, such as the symmetric first oscillation between 3 and 5.5 Å^{-1}. However, several features in the EXAFS spectra of the high As(V) samples are broadened or reduced relative to those of 2LFh, including the prominent oscillations

near 6.2 and 8.3 Å^{-1} and the small oscillations near 5.3 and 7.5 Å^{-1}, which are reduced in the As150 sample and absent in the As150+Ca and As150+Mg samples. Furthermore, the oscillation from 9 to 11 Å^{-1} contains only one broad peak in the EXAFS spectra of the high As(V) samples. The Fourier-transformed EXAFS spectra of the high As(V) samples display a reduced second-shell peak relative to that of 2LFh. The second-shell peak amplitudes decrease

in the order of increasing As(V) uptake (As150 > As150+-Ca ∼ As150+Mg). Because the high initial As(V) samples contain up to 30 mol% As(V), the contribution of Fe–As scattering to the second-shell peak cannot be excluded a priori (nor Fe–P and Fe–Si in the P and Si series). Thus, three overlapping paths can contribute to the second-shell peak of these samples: edge-sharing Fe–Fe, $R \sim 3.0$ Å; corner-sharing Fe–Fe, $R \sim 3.4$ Å; and corner-sharing Fe–As, $R \sim 3.2$–3.3 Å. Shell-by-shell fits of a representative sample in this series (As150+Mg) supported only an edge-sharing Fe–Fe path with $R_{Fe–Fe} = 3.06$ Å ($A = 1.0 \pm 0.2$, $\chi_v^2 = 59.5$) in the second shell (Fig. EA2, Table EA2). Attempts to add an Fe–As path near 3.25 Å corresponding to sorbed As(V) in the ^{2}C geometry or an Fe–Fe path near 3.4 Å corresponding to corner-sharing Fe polyhedra resulted in non-physical (negative) values for A, unreasonable values for R, and an increase in χ_v^2 (see Table EA2). That corner-sharing Fe linkages were not detected by shell-by-shell EXAFS fits in this sample is consistent with previous studies reporting that the presence of As(V) inhibits corner-sharing FeO_6 octahedral linkages during Fe(III) polymerization (Waychunas et al., 1993; Paktunc et al., 2008; Maillot et al., 2013).

3.5.2. Pair distribution function

The PDFs of all the low As(V) samples contain an As–O peak of similar intensity near 1.7 Å. In the As50 PDF, which resembles the 2LFh PDF, the peaks from approximately 2.5–4.0 Å are broadened and overlap more than those of 2LFh. Peaks Fh1–Fh4 of the 2LFh fingerprint appear in the As50 PDF, but the corner-sharing Fe–Fe peak Fh4 is reduced in the As50 sample. Despite the reduced intensity of some characteristic corner-sharing peaks relative to 2LFh, the CSD of the As50 PDF is at least as large as that of 2LFh, suggesting that structural coherence can be maintained even with the loss of some polyhedral connections. Although the As50+Ca and As50+Mg PDFs display fingerprints of Lp, these sample PDFs contain amplitude in the region of 3.2–3.5 Å that is absent in the Lp PDF. Based on the presence of the As–O peak near 1.7 Å, it is likely that sorbed As(V) (R_{As-Fe} of 3.2–3.3 Å, refer to Section 3.2.4) contributes to this amplitude. The presence of Fe–As pairs at this distance can also explain the overlap of the peaks near 3.0 and 3.4 Å in the As50 PDF. Both the As50+Ca and As50+Mg samples contain three peaks from 4.0 to 5.5 Å that are similarly broadened as the high P samples. The Lp1 and Lp4 sheet-stacking peaks are reduced or absent entirely in the As50+Ca and As50+Mg samples, but the amplitudes of these peaks in the As50+Ca PDF are more intense than As50+Mg. The amplitude of the peaks are generally more intense and extend out to higher R in the As50+Ca PDF (CSD > 2.5 nm) relative to the As50+Mg PDF, suggesting more structural coherence in the As50+Ca sample.

The PDFs of the high As(V) samples all display 2LFh-like signatures, but the As150 PDF is the most similar to the PDF of 2LFh. Edge- and corner-sharing Fe–Fe peaks at 3.0 and 3.4 Å are visible in the As150 PDF, but scattering from As–Fe pairs near 3.25 Å obscures the edge-sharing Fe–Fe peak more than in the As50 PDF. The 2LFh fingerprint (peaks Fh1–Fh4) appears in the As150 PDF but peak Fh4 is reduced. Despite the twofold larger As(V) solids ratio in the As150 sample relative to As50, the CSDs of both of these samples are similar. The PDFs of the As150+Ca and As150+Mg samples, which have the highest As(V) solids ratios, have more intense As–O (1.7 Å) and As–Fe (3.25 Å) peaks than the As150 PDF. The As–Fe peak from sorbed As(V) dominates the region from 2.5 to 4.0 Å in the As150+Ca and As150+Mg PDFs, but the width of this peak implies the presence of some additional Fe–Fe pairs in both samples. Beyond 4 Å, the only clear features of the As150+Ca and As150+Mg PDFs are the peaks in the 2LFh fingerprint; however, peak Fh4 vanishes, which is consistent with the reduced intensity of the direct corner-sharing Fe–Fe peak near 3.4 Å. The peaks in the As150+Ca and As150+Mg samples become indiscernible at $R < 1.0$ nm, indicating that the CSD in these samples does not extend beyond 1.0 nm.

3.6. Silicate concentration series

3.6.1. EXAFS spectroscopy

The EXAFS spectra (Fig. 7) of the three low (250Si, 250Si+Ca, 250Si+Mg) and three high (750Si, 750Si+Ca, 750Si+Mg) Si samples all display 2LFh-like fingerprints, including the symmetric first oscillation between 3 and 5.5 Å^{-1}. Several characteristic features of the low and high Si EXAFS spectra are reduced or broadened compared to those of 2LFh, including the intense oscillations near 6.2 and 8.3 Å^{-1} and the small oscillations near 5.3 and 7.5 Å^{-1} indicative of corner-sharing Fe–Fe linkages. The split oscillation from 9 to 11 Å^{-1} in all Si EXAFS spectra is broadened compared to that of 2LFh. The Fourier-transformed EXAFS spectra of the low and high Si samples contain similar first- and second-shell peaks, but the amplitude of the second-shell peak in the low and high Si Fourier-transforms is reduced relative to that of 2LFh. To elucidate the contribution to the second-shell amplitude of a representative sample in the Si series, we attempted to fit the second shell of the Si750+Ca sample with Fe–Fe paths corresponding to both edge- and corner-sharing Fe polyhedra (Fig. EA2 and Table EA2). The fit supported the edge-sharing Fe–Fe path, returning values of 3.06 Å for $R_{Fe–Fe}$ and 1.7 ± 0.1 for A, which are very similar to previous shell-by-shell fit results of Fe(III) precipitates generated in the presence of similar Si (and Ca^{2+}) concentrations (van Genuchten et al., 2012). The attempt to add a corner-sharing path to the fit resulted in a reasonable $R_{Fe–Fe}$ (3.42 Å), but low A with high uncertainty (0.3 ± 0.2). Most importantly, the addition of this corner-sharing Fe path resulted in a larger χ_v^2 value compared to the edge-sharing Fe–Fe path alone, which ultimately fails the test of statistical significance (see Section 2.4). Therefore, the presence of corner-sharing Fe linkages in this representative sample is, at best, ambiguous, if not altogether unsupported by the fit. The absence of corner-sharing Fe polyhedra in Fe(III) precipitates generated in the presence of Si has been reported previously using shell-by-shell EXAFS fits and has been explained by the surface poisoning effects of Si (Doelsch et al., 2000; Pokrovski et al., 2003).

3.6.2. Pair distribution function

All PDFs of the Si concentration series exhibit 2LFh-like fingerprints regardless of the initial Si concentration or the presence of Ca^{2+} or Mg^{2+}. Consistent with the work of Dyer et al. (2012), all PDFs in the Si series display a small Si–O peak near 1.6 Å, an intense Fe–O peak near 2.0 Å and a series of broad overlapping peaks from 3 to 4 Å that are reduced in amplitude relative to 2LFh. The Si–O peak is more defined in the high Si PDFs, which is likely due to the higher Si:Fe solids ratio in these samples. The shape of the edge-sharing Fe–Fe peak near 3.0–3.1 Å is similar in both the low and high Si PDFs, but the low Si PDFs contain more amplitude near the Fe–Fe corner-sharing distance of 3.4 Å. The overlap in the edge- (3.0 Å) and corner-sharing (3.4 Å) Fe–Fe peaks in the Si PDFs is presumably due to atomic pairs involving Si. Similar to P and As(V), Si binds to Fe(III) (oxyhydr)oxides primarily in the ^2C geometry with $R_{Si–Fe}$ near 3.2 Å (Pokrovski et al., 2003; Kanematsu et al., 2013). In this configuration, Si inhibits Fe–Fe corner-sharing linkages, which is consistent with the trends in the amplitude of the 3.4 Å Fe–Fe peak, which decreases in the order of 2LFh > low Si samples > high Si samples. The amplitudes of peaks Fh1–Fh3 of the 2LFh fingerprint are reduced in the high Si samples relative to the low Si samples. Consistent with the decrease in the direct corner-sharing Fe–Fe peak near 3.4 Å, peak Fh4 vanishes in all Si PDFs. The CSD of the Si samples is smaller than in 2LFh, with all peaks disappearing at $R < 1.5$ nm for the low Si samples and $R < 1.2$ nm for the high Si samples.

4. DISCUSSION

4.1. Formation of pseudo-lepidocrocite: the EC precipitate crystalline end-member

In our study, the BgE samples correspond to the material generated under the chemical conditions most favorable for crystal growth. However, systematic changes in characteristic peaks of the BgE sample PDFs relative to the Lp PDF indicate a reduction in sheet-stacking coherence. In a recent study, the EXAFS spectrum of a similar precipitates generated from Fe(II) oxidation in a $NaHCO_3$ electrolyte was fit by linear combinations of Lp, Goe, 2LFh, and Si-HFO reference spectra (Voegelin et al., 2010). The authors hypothesized that the 70% Lp (30% 2LFh+Goe) returned by the fit was due to a minor fraction of Goe (~11%) and (1) the presence of an additional minor, short-ranged phase, or (2) a difference in the crystallinity between the Lp-like sample and Lp reference. Considering the results of Voegelin et al. (2010), we examined the changes to the PDF due to varying mass fractions of Lp and 2LFh (Fig. EA3). We find that none of the analyzed mass ratios of Lp and 2LFh (i.e. 90:10, 75:25, 50:50, or 25:75, or 10:90) could reproduce the PDFs of the BgE samples. Thus, we argue that the deviation in the BgE sample PDFs relative to Lp are best explained by sheet-stacking disorder, rather than the presence of multiple phases. The formation of Goe in the BgE samples is not likely due to the rapid reaction time and the absence of bicarbonate,

although in natural groundwater Goe is more likely to form due to the presence of bicarbonate.

Poor sheet-stacking coherence has been observed in natural and synthetic lepidocrocites (Schwertamnn and Taylor, 1979). Layer-type minerals that have less order along the c-axis relative to the a and b axes are often designated by the "pseudo" prefix, such as the Al oxyhydroxide, pseudo-boehmite (γ-AlOOH), which is isostructural to Lp (Grebille and Berar, 1986). Because a "pseudo"-Lp forms in solutions containing different ion combinations (e.g. NaCl, $CaCl_2$, P50+Mg, P150+Ca, As50+Ca, etc.), it is likely that poor sheet-stacking coherence does not arise exclusively from electrolyte effects hindering inter-sheet H-bonding. Instead, this structural effect might be promoted by the rapid oxidation and polymerization and short reaction stage of our synthesis, which may not provide sufficient time for multiple sheets to orient into coherently scattering stacks.

A lack of coherent sheet stacking is not expected to strongly influence the reactivity of pseudo-Lp precipitates in EC systems based on the site density of different functional groups on the Lp surface. Doubly coordinated oxygens ($>Fe_2OH$) terminating the (001) Lp face are considered inert on Lp as well as other Fe(III) (oxyhydr)oxide minerals (e.g. Goe, 2LFh) (Villalobos et al., 2009; Hiemstra, 2013) due to their stable bond valence (Pauling, 1929). Reactive surface oxygen atoms terminate Lp edges in the (100) and (010) directions and are the surface functional groups expected to undergo ligand exchange with oxyanion adsorptives to form ^2C inner-sphere complexes (Hiemstra, 2013), which is the dominant surface coordination geometry of P, As(V) and Si adsorbed to Fe(III) (oxyhydr)oxide minerals (Pokrovski et al., 2003; Sherman and Randall, 2003; Kwon and Kubicki, 2004; Khare et al., 2007). Thus, low sheet-stacking coherence, which might expose more of the (001) surface to the bulk electrolyte, would not generate more reactive sites than a coherent stack of similar sized sheets assuming similar reactivity at the particle edges. Reactivity is likely to be more dependent on the size of each individual sheet, with a smaller sheet exhibiting more reactive edge sites per mass. Based on the Lp PDF sheet-stacking calculations, the range of structural coherence along the c-axis in the pseudo-Lp samples is ⩽0.7 nm (⩽2 coherent sheets). Consequently, the observed CSD for pseudo-Lp samples (2.5–3.0 nm), which provides a lower bound on particle size (Egami and Billinge, 2003), can yield an upper bound on the number of reactive edge sites.

4.2. P, As(V), and Si oxyanions influence EC precipitate structure differently

Several studies comparing P and As(V) adsorption to preformed Fe(III) (oxyhydr)oxide minerals report similar uptake behavior, competition over surface sites, and similar binuclear ^2C corner-sharing adsorption mechanisms (Manning and Goldberg, 1996; Jain and Loeppert, 2000; Zhao and Stanforth, 2001; Antelo et al., 2005; Zeng et al., 2008). Despite the similar uptake of P and As(V) observed in our study (0.09–0.1 mol:mol for P50 and As50, 0.22–0.24 mol:mol for P150 and As), the P series PDFs indicate

a pseudo-Lp average structure, whereas the As(V) series samples consist of dominant 2LFh-like phases. We argue that the persistence of Lp-like material in the P series arises from the formation of multiple phases, consistent with the sequential uptake of P (Voegelin et al., 2010), whereas the As(V) (and Si) series samples are more likely to consist of a single 2LFh-like phase.

The reactive surface sites of Lp lie on mineral edges in the (1 0 0) and (0 1 0) directions (Venema et al., 1998; Kim et al., 2008). Accordingly, we calculated a maximum P:Fe solids ratio for the pseudo-Lp P150 sample based on the 2.2 nm CSD obtained from the PDF and assuming that only one PO_4 tetrahedron may bind to an FeO_6 octahedron. We estimated that a maximum of 9 PO_4 tetrahedra (5 in the (1 0 0), 4 in the (0 1 0) directions) can adsorb to 2.2 nm diameter pseudo-Lp single sheets consisting of 65 Fe atoms, yielding a P:Fe capacity of 0.14 mol:mol. This calculated maximum adsorption capacity cannot account for the 0.22 mol:mol solids ratio measured in the P150 sample.

The adsorption capacity of poorly crystalline HFO or amorphous Fe(III) polymers coprecipitated in the presence of oxyanions has been reported to approach 0.7 mol:mol (Waychunas et al., 1993). At the onset of electrolysis and Fe(III) precipitation, the P:Fe solution ratio is $\gg 1$, which is consistent with the conditions under which disordered polymers form (Rose et al., 1996, 1997). With hypothetical solids ratios of 0.7 and 0.14 mol:mol for the P–Fe polymers and pseudo-Lp phases, respectively, a material consisting of both 14% polymeric P–Fe phases and 86% pseudo-Lp can account for the 0.22 mol:mol solids ratio observed in the P150 sample. A greater than 85% fraction of pseudo-Lp would make the detection of P–Fe polymers difficult by X-ray techniques that probe the average structure and coordination environment. A similar argument can be made for the formation of multiple phases in the P50 sample, where the initial P:Fe ratio is also large.

In contrast to the P series, the As(V) series is dominated by precipitates with an average 2LFh-like structure. Whereas P and As(V) have similar chemical properties (charge, tetrahedral geometry), there are small differences in their speciation and adsorption equilibrium constants: at pH 7.5 As(V) exists as 85% $HAsO_4^{2-}$ and 15% $H_2AsO_4^-$, P exists as 66% HPO_4^{2-} and 33% $H_2PO_4^-$ (1999); $\log K_{As(V)} = 5.6$; $\log K_P = 5.8$ for sorption to coprecipitated Fe(III) (oxyhydr)oxides (Roberts et al., 2004). The difference in their effect on Fe precipitate structure may also be related to the different sizes of the PO_4 and AsO_4 tetrahedra. The average distance between the oxygen atoms that bind to adjacent Fe polyhedra in the ^2C geometry (tetrahedral vertex to vertex distance) is shorter for P (2.45 Å) (Khare et al., 2007) than for As(V) (2.74 Å) (Kitahama et al., 1975). Consequently, adsorption of PO_4 in the ^2C geometry has been reported to distort adjacent FeO_6 octahedra, which have an O–O distance of approximate 3.0 Å, to accommodate the shorter 2.45 Å O–O distance (Kwon and Kubicki, 2004; Khare et al., 2007). The larger distortion to the FeO_6 octahedra upon PO_4 adsorption can be expected to render crystal growth less favorable in the case of P adsorption, leading to stable P-bearing polymers

consisting of only a few Fe atoms with a large P:Fe ratio. Consistent with our structural data, the large solids ratio of P–Fe polymers would take up significant fractions of P at low Fe doses, leaving the subsequent Fe(III) to polymerize into more crystalline material. In contrast, As(V) adsorption can be expected to cause less distortion in Fe polyhedral bonding, leading to a 2LFh-like structure with more Fe polyhedral linkages than P–Fe polymers. In fact, transmission electron microscopy (TEM) images of Fe(III) precipitates formed in the presence of As(V) (initial As:Fe(III) of 0.13, pH < 4.5) (Paktunc et al., 2008) and P (initial P:Fe(II) of 0.12 and 0.42, pH 7) (Kaegi et al., 2010) show evidence of a single 2LFh-like phase and multi-phase material, respectively.

Despite the lower uptake of Si compared to P or As(V), Si has a greater influence on the resulting average precipitate structure (Si250 is 2LFh-like, P150 is Lp-like), which can be explained by the formation a single Si-HFO phase. Using the Michel model, Hiemstra (2013) reports that 2.5 nm diameter 2LFh particles exhibit a surface site density of approximately 0.6 mol:mol of the singly coordinated oxygen ligand (>FeOH) involved in ^2C binding geometries (Stachowicz et al., 2008; Kanematsu et al., 2013). For the smaller primary crystallite size of our Si samples (CSDs of 1.1–1.5 nm), the measured Si solids ratio can be attained in a single 2LFh-like phase.

Although the initial Si concentration in the Si250 and Si750 samples is higher than the other oxyanion samples, these Si values are representative of the Si content (~ 1 mM) in natural waters (BGS, 2001; Roberts et al., 2004). The abundance of Si relative to P and As(III/V) (Si:P:As $\sim$ 100:10:1), combined with its effects on the formation of EC precipitates, suggest that Si will control the average structure of EC precipitates generated in the field, which is consistent with previous work (Roberts et al., 2004; van Genuchten et al., 2012). Confirming the dominant influence of Si on EC precipitate structure, the PDFs of sludge samples (Section EA5 and Fig. EA4) collected from EC field treatment experiments in an arsenic-affected region of West Bengal, India resemble the Si sample PDFs with reduced CSDs and 2LFh-like fingerprints. Due to both the higher surface site density and specific surface area of 2LFh-like material relative to pseudo-Lp (Hiemstra, 2013), the field treatment sludge and the samples in the Si series should exhibit more reactive sorption sites than pseudo-Lp, which should enhance As(V) uptake given the orders of magnitude higher adsorption affinity of As(V) than Si (Roberts et al., 2004).

4.3. Bivalent cation:oxyanion interaction strongest in order of Ca > Mg; P > As(V) > Si

The >90% removal of P at all initial concentrations in the presence of Ca^{2+}, combined with the near stoichiometric removal of Ca^{2+} in the P250 and P500 samples, points to the strong interaction between Ca^{2+} and P. The structural data from the P series show an increase in precipitate ordering and crystallinity in the presence of Ca^{2+}, which has been explained previously by the formation of P–O–Ca bonds that modify the surface-poisoning behavior of

P during Fe(III) polymerization (Voegelin et al., 2010). Although the same trend of increased P uptake and precipitate ordering is observed in presence of Mg^{2+}, the effects are not as pronounced as observed for Ca^{2+}. Accordingly, the interplay between Mg^{2+} and P during Fe(III) polymerization may involve a larger contribution of electrostatic interactions such as charge screening and electric double layer compression.

Similarly, the change in phase from the 2LFh-like As50 sample to the more crystalline pseudo-Lp As50+Ca and As50+Mg samples suggests the presence of direct As(V)–O–Ca/Mg interactions that can reduce the surface-poisoning effects of As(V). However, the increase in As(V) uptake in the presence of Ca^{2+} and Mg^{2+} is lower than the corresponding increase in P uptake, suggesting a weaker As(V)–Ca/Mg interaction than P–Ca/Mg. Whereas changes in surface charge or double layer thickness might explain the As(V) uptake behavior, the changes in precipitate structure mediated by Ca^{2+} or Mg^{2+} seem to be best-explained by direct As(V)–Ca/Mg association. Given the similar properties of P and As(V) (e.g. charge, tetrahedral coordination), we propose that As(V)–O–Ca bonds, analogous to those formed in the P–Ca system, can form during Fe(III) polymerization, although P likely has a higher affinity than As(V) for Ca coordination. The presence of As–O–Ca linkages have been suggested previously based on systematic changes in the As K-edge EXAFS spectrum of Fe(III) material coprecipitated with As(III) in the presence of Ca^{2+} (Voegelin et al., 2010).

The minor influence of bivalent cations on the uptake and structural effects of Si may be reasoned in terms of decreased electrostatic interactions between Ca^{2+} or Mg^{2+} and the neutral $Si(OH)_4^0$ species. This result is consistent with the negligible effect of bivalent cations on Fe(III) mineral adsorption of As(III), a chemical analog of Si based on its neutral charge ($As(OH)_3^0$) (Kanematsu et al., 2013).

Overall, the uptake and structural data for the P and As(V) series appear to be consistent with stronger Ca–P/As(V) interactions than Mg–P/As(V). Similar trends in enhanced P/As(V) adsorption to goethite in the presence of Ca^{2+} relative to Mg^{2+} have been investigated using charge distribution (CD) and extended triple layer (ETL) surface complexation models. The CD modeling study (Stachowicz et al., 2008) proposes that Ca^{2+} enhances electrostatic interactions by adding more positive charge than Mg^{2+} to the Stern Layer, whereas the ETL modeling study (Kanematsu et al., 2013) suggests the formation of direct Ca–As(V) bonding in ternary surface complexes. In the EC system, the greater influence of Ca^{2+} than Mg^{2+} on Fe(III) precipitate structure and uptake of P/As(V) is consistent with the formation of some direct cation–oxyanion bonding in the Ca^{2+} and As(V)/P system, which is expected to be stronger than the electrostatic interactions presumably dominating in the Mg^{2+} and As(V)/P systems. Although electrostatics may play a major role in both the Ca^{2+} and Mg^{2+} systems, the lower ionic potential of Ca^{2+} (charge/ionic radius), which favors stronger covalent-type bonding, can explain the larger impact of Ca^{2+} relative to Mg^{2+}.

With regards to the application of EC in field treatment, the role of bivalent cations is complex. Here we show that bivalent cations ($Ca^{2+} > Mg^{2+}$) increase oxyanion uptake (P > As(V) > Si) per mass of Fe, presumably by a combination of electrostatic interactions and direct bonding to As(V)/P. However, Ca^{2+} has also been reported to decrease the efficiency of arsenic uptake by Fe(III) (oxyhydr)oxides in waters with high HCO_3^-/CO_3^{2-} by leading to $CaCO_{3(s)}$ formation, which can associate with Fe(III) (oxyhydr)oxides and block reactive surface sites (Saalfield and Bostick, 2010). Another aspect of field treatment influenced by the interaction of bivalent cations and oxyanions is the low-cost separation of oxyanion-bearing precipitates, which is a challenge facing current EC operation (Amrose et al., 2013). Whereas oxyanions reduce EC precipitate crystallite size and lead to colloidally stable suspensions (Fig. 1), bivalent cations can both indirectly increase crystallite size (P and As(V) series) and promote crystallite aggregation, which increases settling velocity and facilitates particle separation by low-cost gravitational settling.

In the context of particle separation, crystallite size as probed by molecular scale techniques (PDF) should be distinguished from aggregated floc size as probed by macroscopic techniques (turbidity). Because the PDF is only sensitive to coherent atomic ordering, the CSD derived from the decay in the PDF provides a lower limit on particle size. The aggregation of primary crystallites or the formation of an amorphous surface layer, for instance, do not appear in the PDF, but are key physicochemical properties that influence macroscopic behaviors like particle settling velocity. Although we show that bivalent cations can increase the CSD and lead to more crystalline material, larger and more ordered crystallites do not necessarily have increased settling velocities or ease of separation. For instance, the As150+Ca/Mg samples, which have the smallest CSDs in our study, settle more quickly than the P150 and As150 samples.

4.4. Insights into the polyhedral connectivity of oxyanion-bearing HFO

Due to their influence on the mobility and bioavailability of contaminants and nutrients, short-ranged Fe(III) polymers that form in the presence of P, As(III,V), and Si (i.e. P-HFO, As-HFO, Si-HFO and/or amorphous Fe–As/P phases) have been the focus of intense research (e.g. (Waychunas et al., 1993; Rose et al., 1996; Pokrovski et al., 2003)). The structures of high oxyanion-bearing Fe(III) precipitates are reported to differ relative to lab-synthesized 2LFh based on a reduction in corner-sharing linkages as inferred from XAS analysis, consistent with our shell-by-shell fits of As150+Mg and Si750+Ca samples. However, describing the polyhedral connectivity of HFO and/or amorphous Fe–As/P phases using shell-by-shell EXAFS fits alone can be limited by the presence of multiple atomic paths that contribute to the broad second-shell peak of the Fourier-transformed EXAFS spectra.

Our study demonstrates that the PDF technique can be used to better understand the polyhedral connectivity of poorly-ordered materials that can be difficult to interpret using EXAFS spectroscopy. Despite differences in initial electrolyte composition and local (1–4 Å) bonding

environments as evidenced in the PDF, the most disordered 2LFh-like samples (e.g. As150+Ca/Mg; Si750+Ca/Mg) share similar intermediate ranged correlations, suggesting that these samples contain a similar "backbone" of coherently-scattering atomic clusters that are present in lab-synthesized 2LFh. The fact that peaks Fh1–Fh3 in the 2LFh fingerprint appear in both the Si and As series confirms that these peaks do not arise from atomic pairs involving Si or As because a shift in peak position would be apparent due to the difference in the sizes of the SiO_4 ($R_{Si-O} \sim 1.6$ Å) and AsO_4 ($R_{As-O} \sim 1.7$ Å) tetrahedra. Based on the model refinement for 2LFh, peaks Fh1 and Fh3 in the PDFs of 2LFh-like samples can be assigned to edge-sharing Fe polyhedra within an edge-sharing sheet (site Fe1), whereas peak Fh2 (and Fh4 when present) arises from corner-sharing polyhedral (sites Fe2 and Fe3) sitting atop vacancies in the edge-sharing sheet. However, as determined by shell-by-shell fits, a significant contribution of corner-sharing Fe linkages was not detected in the corresponding Fourier-transformed EXAFS spectra of identical samples. Thus, structural models derived from EXAFS analysis alone that propose the presence of only edge-sharing Fe–Fe polyhedra may not provide a complete description of the atomic arrangement, which in our samples requires a fraction of Fe to be in corner-sharing bonding environments, as evidenced by the presence of peak Fh2 (and Fh4) in the 2LFh fingerprint.

In our most disordered samples (As150+Ca/Mg; Si750+Ca/Mg), when peaks Fh1, Fh2, and Fh3 decrease relative to these peaks in 2LFh, they do so almost uniformly, whereas peak Fh4 and the direct corner-sharing Fe–Fe peak near 3.4 Å do so disproportionally. Because the corner-sharing linkage between sites Fe2 and Fe3 (corner-sharing FeO_6 and FeO_4, respectively), does not contribute to Fh2 (see Fig. 5), the disproportionate reduction in intensity of Fh4 and the direct corner-sharing peak relative to Fh2 can be explained by a decrease in the occupancy of sites Fe2 and Fe3. This decrease in Fe2 and Fe3 site occupancy is consistent with a recent study showing that the surface of 2LFh consists of depleted Fe2 and Fe3 sites, whereas these same sites in the 2LFh mineral core are defect-free (Hiemstra, 2013). The <1.0 nm CSD of our most disordered samples points to a large surface to core ratio, which would lead to a dramatic depletion of the Fe2 and Fe3 sites. Moreover, we expect that oxyanion adsorption is energetically favorable at the edge-sharing 6-membered ring vacancy (Auffan et al., 2008), which is the location of the Fe2 and Fe3 sites. Consequently, the presence of P, As(V), and Si, well-known to inhibit corner-sharing Fe linkages, likely increase the depletion of the Fe2 and Fe3 sites by competing with Fe polyhedra for the six-membered ring vacancy during Fe(III) polymerization.

5. CONCLUSIONS

Our study shows that the electrolyte composition strongly determines the structure, ion uptake behavior, and colloidal stability of the Fe(III) precipitates generated by the electrolytic dissolution of Fe(0) electrodes. In the absence of strongly adsorbing ions, a Lp-like precipitate with poor sheet stacking coherence (pseudo-Lp) forms. The presence of P, As(V), and Si oxyanions influences the resulting structure differently. Despite the similar uptake of P and As(V), precipitates dominated by pseudo-Lp signatures forms in the presence of P (initial P:Fe = 0.1 and 0.3), whereas the presence of As(V) leads to predominantly 2LFh-like phases (initial As:Fe = 0.1 and 0.3). In the Si series, a 2LFh-like material is produced in all analyzed samples even though the uptake of Si is less than in samples having the same initial concentrations of P and As(V). In this study, we show that the presence of bivalent cations (1) enhances oxyanion uptake, (2) increases the aggregated particle size as measured by settled turbidity, and (3) alters mineral phase and primary crystallite size. Our results suggest a systematic decrease in the strength of bivalent cation:oxyanion interactions in the order of $Ca^{2+} > Mg^{2+}$ and $P > As(V) \gg Si$. We are able to interpret the intermediate-ranged region of the PDF of the most disordered oxyanion-bearing Fe(III) precipitate samples using the Michel model. Despite the deficiency of corner-sharing Fe polyhedra in some of our most disordered samples as determined from shell-by-shell EXAFS fits, the corresponding PDFs contain peaks attributed to corner-sharing polyhedra at interatomic distances beyond the range available using EXAFS spectroscopy. We attribute the decrease in corner-sharing Fe polyhedra in these samples relative to the reference 2LFh to a reduction of surface Fe2 and Fe3 sites, likely promoted by the presence of strongly adsorbing oxyanions binding at these locations, whereas the precipitate core contains a higher Fe2 and Fe3 site occupancy.

APPENDIX A. SUPPLEMENTARY DATA

Supplementary data associated with this article can be found, in the online version, at http://dx.doi.org/10.1016/j.gca.2013.11.044.

REFERENCES

Anon. (1999) *CRC Handbook of Chemistry and Physics*. Boca Raton, FL: Chapman and Hall/CRCnetBASE.

Amrose S., Gadgil A., Srinivasan V., Kowolik K., Muller M., Huang J. and Kostecki R. (2013) Arsenic removal from groundwater using iron electrocoagulation: effect of charge dosage rate. *J Environ Sci Health A* **48**(9), 1019–1030.

Antelo J., Avena M., Fiol S., Lopez R. and Arce F. (2005) Effects of pH and ionic strength on the adsorption of phosphate and arsenate at the goethite–water interface. *J. Colloid Interface Sci.* **285**(2), 476–486.

Auffan M., Rose J., Proux O., Borschneck D., Masion A., Chaurand P., Hazemann J., Chaneac C., Jolivet J., Wiesner M., Van Geen A. and Bottero J. (2008) Enhanced adsorption of arsenic onto maghemites nanoparticles: As(III) as a probe of the surface structure and heterogeneity. *Langmuir*, 3215–3222.

Bard A. J. and Faulkner L. R. (2001). , p. 833.

BGS (2001) *Arsenic Contamination of Groundwater in Bangladesh.* .

Caetano M. and Vale C. (2002) Retention of arsenic and phosphorus in iron-rich concretions of Tagus salt marshes. *Mar. Chem.* **79**(3–4), 261–271.

Chupas P., Qiu X., Hanson J., Lee P., Grey C. and Billinge S. (2003) Rapid-acquisition pair distribution function (RA-PDF) analysis. *J. Appl. Crystallogr.* **36**, 1342–1347.

Cismasu A., Michel F., Stebbins J., Levard C. and Brown G. (2012) Properties of impurity-bearing ferrihydrite I. Effects of Al content and precipitation rate on the structure of 2-line ferrihydrite. *Geochim. Cosmochim. Acta* **92**, 275–291.

Cismasu A., Michel F., Tcaciuc A., Tyliszczak T. and Brown G. (2011) Composition and structural aspects of naturally occurring ferrihydrite. *C.R. Geosci.* **343**(2–3), 210–218.

Doelsch E., Rose J., Masion A., Bottero J. Y., Nahon D. and Bertsch P. M. (2000) Speciation and crystal chemistry of iron(III) chloride hydrolyzed in the presence of SiO$_4$ ligands. 1. An FeK-edge EXAFS study. *Langmuir* **16**(10), 4726–4731.

Drits V., Sakharov B., Salyn A. and Manceau A. (1993) Structural model for ferrihydrite. *Clay Miner.* **28**(2), 185–207.

Dyer L., Chapman K., English P., Saunders M. and Richmond W. (2012) Insights into the crystal and aggregate structure of Fe3+ oxide/silica co-precipitates. *Am. Mineral.* **97**(1), 63–69.

Egami T. and Billinge S. J. L. (2003) *Underneath the Bragg Peaks: Structural Analysis of Complex Materials.* (xviii, 440pp).

Farrow C., Juhas P., Liu J., Bryndin D., Bozin E., Bloch J., Proffen T. and Billinge S. (2007) PDFfit2 and PDFgui: computer programs for studying nanostructure in crystals. *J. Phys. Condens. Matter* **19**(33).

Grebille D. and Berar J. (1986) Calculation of diffraction line profiles in the case of coupled stacking-fault and size-effect broadening – application to boehmite AlOOH. *J. Appl. Crystallogr.* **19**, 249–254.

Gualtieri A. and Venturelli P. (1999) In situ study of the goethite–hematite phase transformation by real time synchrotron powder diffraction. *Am. Mineral.*, 895–904.

Guan X., Ma J., Dong H. and Jiang L. (2009) Removal of arsenic from water: effect of calcium ions on As(III) removal in the KMnO(4)–Fe(II) process. *Water Res.* **43**(20), 5119–5128.

Gustafsson J. P. (2013). .

Guyodo Y., Sainctavit P., Arrio M. A., Carvallo C., Penn R. L., Erbs J. J., Forsberg B. S., Morin G., Maillot F., Lagroix F., Bonville P., Wilhelm F. and Rogalev A. (2012) X-ray magnetic circular dichroism provides strong evidence for tetrahedral iron in ferrihydrite. *Geochem. Geophys. Geosyst.* **13**.

Hammersley A., Svensson S., Hanfland M., Fitch A. and Hausermann D. (1996) Two-dimensional detector software: from real detector to idealised image or two-theta scan. *High Pressure Res*, 235–248.

Han F., Su Y., Monts D., Plodinec M., Banin A. and Triplett G. (2003) Assessment of global industrial-age anthropogenic arsenic contamination. *Naturwissenschaften* **90**(9), 395–401.

Harrington R., Hausner D., Xu W., Bhandari N., Michel F., Brown G., Strongin D. and Parise J. (2011) Neutron pair distribution function study of two-line ferrihydrite. *Environ. Sci. Technol.* **45**(23), 9883–9890.

Hiemstra T. (2013) Surface and mineral structure of ferrihydrite. *Geochim. Cosmochim. Acta* **105**, 316–325.

Jain A. and Loeppert R. H. (2000) Effect of competing anions on the adsorption of arsenate and arsenite by ferrihydrite. *J. Environ. Qual.* **29**(5), 1422–1430.

Jia Y. and Demopoulos G. (2008) Coprecipitation of arsenate with iron(III) in aqueous sulfate media: effect of time, lime as base and co-ions on arsenic retention. *Water Res.* **42**(3), 661–668.

Kaegi R., Voegelin A., Folini D. and Hug S. J. (2010) Effect of phosphate, silicate, and Ca on the morphology, structure and elemental composition of Fe(III)-precipitates formed in aerated Fe(II) and As(III) containing water. *Geochim. Cosmochim. Acta* **74**(20), 5798–5816.

Kanematsu M., Young T. M., Fukushi K., Green P. G. and Darby J. L. (2010) Extended triple layer modeling of arsenate and phosphate adsorption on a goethite-based granular porous adsorbent. *Environ. Sci. Technol.* **44**(9), 3388–3394.

Kanematsu M., Young T. M., Fukushi K., Green P. G. and Darby J. L. (2013) Arsenic(III, V) adsorption on a goethite-based adsorbent in the presence of major co-existing ions: modeling competitive adsorption consistent with spectroscopic and molecular evidence. *Geochim. Cosmochim. Acta* **106**, 404–428.

Kelly S. D., Hesterberg D. and Ravel B. (2008) Analysis of soils and minerals using X-ray absorption spectroscopy. In *Methods of Soil Analysis. Part 5. Mineralogical Methods. SSA Book Series*, No. 5, Soil Science Society of America.

Khare N., Martin J. D. and Hesterberg D. (2007) Phosphate bonding configuration on ferrihydrite based on molecular orbital calculations and XANES fingerprinting. *Geochim. Cosmochim. Acta* **71**(18), 4405–4415.

Kim J., Nielsen U. G. and Grey C. P. (2008) Local environments and lithium adsorption on the iron oxyhydroxides lepidocrocite (gamma-FeOOH) and goethite (alpha-FeOOH): a H-2 and Li-7 solid-state MAS NMR study. *J. Am. Chem. Soc.* **130**(4), 1285–1295.

Kitahama K., Kiriyama R. and Baba Y. (1975) Refinement of crystal-structure of scorodite. *Acta Crystallogr. Sect. B Struct. Sci.*, 322–324.

Kuhn A. and Sigg L. (1993) Arsenic cycling in eutrophic lake Greifen, Switzerland – influence of seasonal redox processes. *Limnol. Oceanogr.* **38**(5), 1052–1059.

Kumar P. R., Chaudhari S., Khilar K. C. and Mahajan S. P. (2004) Removal of arsenic from water by electrocoagulation. *Chemosphere* **55**(9), 1245–1252.

Kwon K. D. and Kubicki J. D. (2004) Molecular orbital theory study on surface complex structures of phosphates to iron hydroxides: calculation of vibrational frequencies and adsorption energies. *Langmuir* **20**(21), 9249–9254.

Lakshmanan D., Clifford D. and Samanta G. (2010) Comparative study of arsenic removal by iron using electrocoagulation and chemical coagulation. *Water Res.*, 5641–5652.

Lakshmanan D., Clifford D. A. and Samanta G. (2009) Ferrous and ferric ion generation during iron electrocoagulation. *Environ. Sci. Technol.* **43**(10), 3853–3859.

Li L., van Genuchten C. M., Addy S. E. A., Yao J., Gao N. and Gadgil A. J. (2012) Modeling As(III) oxidation and removal with iron electrocoagulation in groundwater. *Environ. Sci. Technol.* **46**(21), 12038–12045.

Maillot F., Morin G., Juillot F., Bruneel O., Casiot C., Ona-Nguema G., Wang Y., Lebrun S., Aubry E., Vlaic G. and Brown G. (2013) Structure and reactivity of As(III)- and As(V)-rich schwertmannites and amorphous ferric arsenate sulfate

from the Carnoules acid mine drainage, France. Comparison with biotic and abiotic model compounds and implications for As remediation. *Geochim. Cosmochim. Acta* **104**, 310–329.

Maillot F., Morin G., Wang Y., Bonnin D., Ildefonse P., Chaneac C. and Calas G. (2011) New insight into the structure of nanocrystalline ferrihydrite: EXAFS evidence for tetrahedrally coordinated iron(III). *Geochim. Cosmochim. Acta* **75**(10), 2708–2720.

Manceau A. (2009) Evaluation of the structural model for ferrihydrite derived from real-space modelling of high-energy X-ray diffraction data. *Clay Miner.* **44**(1), 19–34.

Manceau A. (2011) Critical evaluation of the revised akdalaite model for ferrihydrite. *Am. Mineral.* **96**(4), 521–533.

Manceau A. (2012) Comment on "Direct observation of tetrahedrally coordinated Fe(III) in ferrihydrite". *Environ. Sci. Technol.* **46**(12), 6882–6884.

Manceau A. and Gates W. (2013) Incorporation of Al in iron oxyhydroxides: implications for the structure of ferrihydrite. *Clay Miner.* **48**(3), 481–489.

Manning B. A. and Goldberg S. (1996) Modeling competitive adsorption of arsenate with phosphate and molybdate on oxide minerals. *Soil Sci. Soc. Am. J.* **60**(1), 121–131.

Masue Y., Loeppert R. H. and Kramer T. A. (2007) Arsenate and arsenite adsorption and desorption behavior on coprecipitated aluminum: iron hydroxides. *Environ. Sci. Technol.* **41**(3), 837–842.

Michel F., Barron V., Torrent J., Morales M., Serna C., Boily J., Liu Q., Ambrosini A., Cismasu A. and Brown G. (2010) Ordered ferrimagnetic form of ferrihydrite reveals links among structure, composition, and magnetism. *Proc. Nat. Acad. Sci. U.S.A.* **107**(7), 2787–2792.

Michel F. M., Ehm L., Antao S. M., Lee P. L., Chupas P. J., Liu G., Strongin D. R., Schoonen M. A. A., Phillips B. L. and Parise J. B. (2007a) The structure of ferrihydrite, a nanocrystalline material. *Science* **316**(5832), 1726–1729.

Michel F. M., Ehm L., Liu G., Han W. Q., Antao S. M., Chupas P. J., Lee P. L., Knorr K., Eulert H., Kim J., Grey C. P., Celestian A. J., Gillow J., Schoonen M. A. A., Strongin D. R. and Parise J. B. (2007b) Similarities in 2-and 6-line ferrihydrite based on pair distribution function analysis of X-ray total scattering. *Chem. Mater.* **19**(6), 1489–1496.

Newville M. (2001) IFEFFIT: interactive XAFS analysis and FEFF fitting. *J. Synchrotron Radiat.*, 322–324.

Nordstrom D. (2002) Public health – worldwide occurrences of arsenic in ground water. *Science* **296**(5576), 2143–2145.

Paktunc D., Dutrizac J. and Gertsman V. (2008) Synthesis and phase transformations involving scorodite, ferric arsenate and arsenical ferrihydrite: implications for arsenic mobility. *Geochim. Cosmochim. Acta*, 2649–2672.

Paktunc D., Manceau A. and Dutrizac J. (2013) Incorporation of Ge in ferrihydrite: implications for the structure of ferrihydrite. *Am. Mineral.* **98**(5–6), 848–858.

Pauling L. (1929) The principles determining the structure of complex ionic crystals. *J. Am. Chem. Soc.* **51**, 1010–1026.

Peak D. and Regier T. (2012) Direct observation of tetrahedrally coordinated Fe(III) in ferrihydrite. *Environ. Sci. Technol.* **46**(6), 3163–3168.

Petkov V. (2005) Atomic-scale structure of nanocrystals by the atomic pair distribution function technique. *Mol. Simul.* **31**(2–3), 101–105.

Pokrovski G. S., Schott J., Garges F. and Hazemann J. L. (2003) Iron (III)-silica interactions in aqueous solution: insights from X-ray absorption fine structure spectroscopy. *Geochim. Cosmochim. Acta* **67**(19), 3559–3573.

Proffen T., Billinge S. J. L., Egami T. and Louca D. (2003) Structural analysis of complex materials using the atomic pair distribution function – a practical guide. *Z. Kristallogr.* **218**(2), 132–143.

Rahman M. (2002) Arsenic and contamination of drinking-water in Bangladesh: a public-health perspective. *J. Health Popul. Nutr.* **20**(3), 193–197.

Rancourt D. G., Fortin D., Pichler T., Thibault P. J., Lamarche G., Morris R. V. and Mercier P. H. J. (2001) Mineralogy of a natural As-rich hydrous ferric oxide coprecipitate formed by mixing of hydrothermal fluid and seawater: implications regarding surface complexation and color banding in ferrihydrite deposits. *Am. Mineral.* **86**(7–8), 834–851.

Roberts L. C., Hug S. J., Ruettimann T., Billah M., Khan A. W. and Rahman M. T. (2004) Arsenic removal with iron(II) and iron(III) waters with high silicate and phosphate concentrations. *Environ. Sci. Technol.* **38**(1), 307–315.

Rose J., Flank A. M., Masion A., Bottero J. Y. and Elmerich P. (1997) Nucleation and growth mechanisms of Fe oxyhydroxide in the presence of PO_4 ions. 2. P K-edge EXAFS study. *Langmuir* **13**(6), 1827–1834.

Rose J., Manceau A., Bottero J. Y., Masion A. and Garcia F. (1996) Nucleation and growth mechanisms of Fe oxyhydroxide in the presence of PO_4 ions. 1. Fe K-edge EXAFS study. *Langmuir* **12**(26), 6701–6707.

Saalfield S. L. and Bostick B. C. (2010) Synergistic effect of calcium and bicarbonate in enhancing arsenate release from ferrihydrite. *Geochim. Cosmochim. Acta* **74**(18), 5171–5186.

Schwertmann U. and Cornell R. M. (1991) *Iron Oxides in the Laboratory: Preparation and Characterization.* VCH, Weinheim; New York (xiv, 137pp).

Sherman D. M. and Randall S. R. (2003) Surface complexation of arsenie(V) to iron(III) (hydr)oxides: structural mechanism from ab initio molecular geometries and EXAFS spectroscopy. *Geochim. Cosmochim. Acta* **67**(22), 4223–4230.

Sposito G. (2008) *The Chemistry of Soils.* Oxford University Press, Oxford; New York (xii, 329pp).

Stachowicz M., Hiemstra T. and van Riemsdijk W. H. (2008) Multi-competitive interaction of As(III) and As(V) oxyanions with Ca^{2+}, Mg^{2+}, PO_4^{3-}, and CO_3^{2-} ions on goethite. *J. Colloid Interface Sci.* **320**(2), 400–414.

Stumm W. and Lee G. (1961) Oxygenation of ferrous iron. *Ind. Eng. Chem.* **53**(2), 143–146.

Sverjensky D. A. (2006) Prediction of the speciation of alkaline earths adsorbed on mineral surfaces in salt solutions. *Geochim. Cosmochim. Acta* **70**(10), 2427–2453.

Toner B. M., Berquo T. S., Michel F. M., Sorensen J. V., Templeton A. S. and Edwards K. J. (2012) Mineralogy of iron microbial mats from Loihi Seamount. *Front. Microbiol.* **3**, 118.

van Genuchten C., Addy S., Pena J. and Gadgil A. (2012) Removing arsenic from synthetic groundwater with iron electrocoagulation: an Fe and As K-edge EXAFS study. *Environ. Sci. Technol.* **46**(2), 986–994.

Venema P., Hiemstra T., Weidler P. G. and van Riemsdijk W. H. (1998) Intrinsic proton affinity of reactive surface groups of metal (hydr)oxides: application to iron (hydr)oxides. *J. Colloid Interface Sci.* **198**(2), 282–295.

Villalobos M., Cheney M. A. and Alcaraz-Cienfuegos J. (2009) Goethite surface reactivity: II. A microscopic site-density model that describes its surface area-normalized variability. *J. Colloid Interface Sci.* **336**(2), 412–422.

Voegelin A., Kaegi R., Frommer J., Vantelon D. and Hug S. J. (2010) Effect of phosphate, silicate, and Ca on Fe(III)-precipitates formed in aerated Fe(II)- and As(III)-containing water studied by X-ray absorption spectroscopy. *Geochim. Cosmochim. Acta* **74**(1), 164–186.

Waychunas G. A., Rea B. A., Fuller C. C. and Davis J. A. (1993) Surface-chemistry of ferrihydrite. 1. EXAFS studies of the

geometry of coprecipitated and adsorbed arsenate. *Geochim. Cosmochim. Acta* **57**(10), 2251–2269.

Webb S. (2005) SIXPACK: a graphical user interface for XAS analysis using IFEFFIT. *Phys. Scripta* **T115**, 1011–1014.

Wilkie J. A. and Hering J. G. (1996) Adsorption of arsenic onto hydrous ferric oxide: effects of adsorbate/adsorbent ratios and co-occurring solutes. *Colloids Surf. A Physicochem. Eng. Aspects* **107**, 97–110.

Wyckoff R. W. G. (1963) Crystal Structures, vol. 1. Interscience Publishers, New York, p. 290–295.

Zeng H., Fisher B. and Giammar D. E. (2008) Individual and competitive adsorption of arsenate and phosphate to a high-surface-area iron oxide-based sorbent. *Environ. Sci. Technol.* **42**(1), 147–152.

Zhao H. S. and Stanforth R. (2001) Competitive adsorption of phosphate and arsenate on goethite. *Environ. Sci. Technol.* **35**(24), 4753–4757.

Associate editor: Nita Sahai